New Journal of Physics
The open access journal at the forefront of physics

Deutsche Physikalische Gesellschaft DPG IOP Institute of Physics

PAPER • OPEN ACCESS

Feynman-diagrams approach to the quantum Rabi model for ultrastrong cavity QED: stimulated emission and reabsorption of virtual particles dressing a physical excitation

To cite this article: Omar Di Stefano *et al* 2017 *New J. Phys.* **19** 053010

New Journal of Physics
The open access journal at the forefront of physics

Deutsche Physikalische Gesellschaft DPG
IOP Institute of Physics

Published in partnership with: Deutsche Physikalische Gesellschaft and the Institute of Physics

OPEN ACCESS

RECEIVED
30 January 2017

REVISED
27 March 2017

ACCEPTED FOR PUBLICATION
12 April 2017

PUBLISHED
16 May 2017

PAPER

Feynman-diagrams approach to the quantum Rabi model for ultrastrong cavity QED: stimulated emission and reabsorption of virtual particles dressing a physical excitation

Omar Di Stefano[1,2,5], **Roberto Stassi**[2], **Luigi Garziano**[3], **Anton Frisk Kockum**[2], **Salvatore Savasta**[1,2] **and Franco Nori**[2,4]

[1] MIFT—Dipartimento di Scienze Matematiche e Informatiche Scienze Fisiche e Scienze della Terra, Università di Messina, I-98166 Messina, Italy
[2] CEMS, RIKEN, Saitama 351-0198, Japan
[3] University of Southampton, Southampton, SO17 1BJ, United Kingdom
[4] Physics Department, The University of Michigan, Ann Arbor, Michigan 48109-1040, United States of America
[5] Author to whom any correspondence should be addressed.

E-mail: email: odistefano@unime.it

Keywords: ultrastrong-coupling regime, virtual particles, Feynman diagrams, cavity-QED, quantum vacuum fluctuations, three-level quantum system

Abstract

In quantum field theory, bare particles are dressed by a cloud of virtual particles to form physical particles. The virtual particles affect properties such as the mass and charge of the physical particles, and it is only these modified properties that can be measured in experiments, not the properties of the bare particles. The influence of virtual particles is prominent in the ultrastrong-coupling regime of cavity quantum electrodynamics (QED), which has recently been realised in several condensed-matter systems. In some of these systems, the effective interaction between atom-like transitions and the cavity photons can be switched on or off by external control pulses. This offers unprecedented possibilities for exploring quantum vacuum fluctuations and the relation between physical and bare particles. We consider a single three-level quantum system coupled to an optical resonator. Here we show that, by applying external electromagnetic pulses of suitable amplitude and frequency, each virtual photon dressing a physical excitation in cavity-QED systems can be converted into a physical observable photon, and back again. In this way, the hidden relationship between the bare and the physical excitations can be unravelled and becomes experimentally testable. The conversion between virtual and physical photons can be clearly pictured using Feynman diagrams with cut loops.

1. Introduction

In quantum field theory (QFT), the creation and annihilation operators in the Lagrangian describe the creation and destruction of *bare* particles which, however, can not be directly observed in experiments (see, e.g., [1, 2]). Bare particles, due to the interaction terms in the Lagrangian, are actually *dressed* by *virtual* particles and become real *physical* particles which can be detected. The interaction modifies the properties of the particles, e.g., giving rise to the Lamb shift of electronic energy levels [3, 4] and affecting the charge, mass, and magnetic moment of the electron [1, 5, 6]. The predictions of the theory must be expressed in terms of the properties of the physical particles, not of the non-interacting (or bare) particles [1, 2]. The relations between the bare and the physical particles are unobservable.

The influence of virtual particles features prominently in the ultrastrong coupling (USC) regime of cavity quantum electrodynamics (QED) [7, 8]. In cavity QED [9], the interaction between light confined in a reflective cavity and natural or artificial atoms is studied in conditions where the quantum nature of light is important. The system enters the USC regime when the light–matter coupling rate becomes an appreciable fraction of the unperturbed resonance frequencies of the photons and the atom. In this regime, the routinely-invoked rotating

wave approximation (RWA) is no longer applicable and the counter-rotating terms in the light–matter interaction significantly change the standard cavity QED scenario [7, 8, 10–22]. For example, very recently it has been shown that, in the USC regime, a single photon can excite two or more atoms [21]. This effect can occur because the atom-cavity system can essentially borrow the needed second virtual photon from the quantum vacuum. In the past few years, the USC regime has been reached experimentally in a variety of solid-state systems and spectral ranges [23–37].

The need to distinguish between virtual and physical particles in the USC regime of cavity QED is exemplified by the fact that the correct description of the output photon flux from the cavity, as well as of higher-order Glauber normal-order correlation functions, requires a proper generalisation of input–output theory [15, 38]. Due to the contribution from counter-rotating terms in the interaction Hamiltonian, the ground state $|E_0\rangle$ of the system contains a finite number of photons [39], i.e.,

$$\langle E_0 \, |\hat{a}^\dagger \hat{a}| \, E_0\rangle \neq 0,$$

where $\hat{a}$ and $\hat{a}^\dagger$ are the annihilation and creation operators for the cavity mode. However, the ground state can not emit energy, so the output photon flux can not be proportional to $\langle \hat{a}^\dagger \hat{a}\rangle$, as in standard input–output theory. Instead, it has been shown [15, 40] that the cavity output (which can be detected by a photo-absorber) is proportional to $\langle \hat{x}^- \hat{x}^+\rangle$, where $\hat{x}^+$ is the positive frequency component of the quadrature operator $\hat{x} = \hat{a} + \hat{a}^\dagger$ and $\hat{x}^- = (\hat{x}^+)^\dagger$. The result

$$\langle E_0 \, |\hat{x}^- \hat{x}^+| \, E_0\rangle = 0$$

demonstrates that the photons that contribute to the ground state are not observable physical particles. An analogous situation arises when the photons are coupled to collective matter excitations described by bosonic fields [41]. It can also be shown that the (physical) system excitations are enriched by unobservable virtual particles. For instance, the first excited state, corresponding to a single physical particle, may contain contributions from an odd number of excitations. All these unobservable contributions, however, are significant only in the USC regime, not at weaker coupling strengths. An interesting feature of these condensed-matter systems is that the effective interaction between atom-like transitions and the cavity field can be switched on and off by applying external drives. This offers the opportunity to convert the virtual excitations into real particles which can then be detected. Both spontaneous [7] and optically [42] or electrically [43] stimulated conversion of virtual photons from the ground state of a cavity QED system in the USC regime have recently been analysed. Also, virtual photon pairs are converted into real ones in the dynamical Casimir effect (DCE) [44], which has been analysed [45–47] and experimentally demonstrated [48] in circuit QED. Potentially, a proper modulation of an effective mirror (i.e., an oscillating boundary condition) in a DCE setup could also allow for absorption of photon pairs [49].

Here we show how to convert various numbers of virtual photons into real ones and back, both for the dressed vacuum state and for a dressed excited state, in a three-level system with one transition ultrastrongly coupled to an optical resonator. We also show that the corresponding Feynman diagrams can be obtained by cutting the loop diagrams describing the energy correction of a physical excitation. Specifically, conversion of virtual photons dressing a physical excitation into real ones is described by the first half of cut loop-diagrams (photon emission). Similarly, the conversion of real photons back into virtual ones bound to a physical excitation corresponds to the second half (photon absorption). Moreover, the proposed scheme does not require the ultrafast modulation of boundary conditions and it can give rise to a conversion probability close to one.

2. Results

2.1. The quantum Rabi model

The simplest cavity-QED model beyond the RWA is the quantum Rabi model [50, 51]. The Hamiltonian is ($\hbar = 1$) $\hat{H}_{\rm R} = \hat{H}_0 + \hat{V}$, where $\hat{H}_0 = \omega_{\rm c}\hat{a}^\dagger\hat{a} + \omega_e \, |e\rangle\langle e| + \omega_g \, |g\rangle\langle g|$ is the bare Hamiltonian in the absence of interaction. Here, $\hat{a}$ and $\hat{a}^\dagger$ are the photon destruction and creation operators for the cavity mode with resonance frequency $\omega_{\rm c}$; $|g\rangle$ and $|e\rangle$ are the ground and excited atomic states, respectively, and $\omega_{e(g)}$ are the corresponding energy eigenvalues. The interaction Hamiltonian is

$$\hat{V} = \Omega_{\rm R}(\hat{a}^\dagger + \hat{a})\hat{\sigma}_x, \tag{1}$$

where $\Omega_{\rm R}$ is the coupling strength and $\hat{\sigma}_x = \hat{\sigma}_+ + \hat{\sigma}_- = |e\rangle\langle g| + |g\rangle\langle e|$. When $\omega_{\rm c} \approx \omega_{eg} \equiv \omega_e - \omega_g$, the interaction Hamiltonian can be separated into a resonant and a non-resonant part: $\hat{V} = \hat{V}_{\rm r} + \hat{V}_{\rm nr}$, where $\hat{V}_{\rm r} = \Omega_{\rm R}(\hat{a}^\dagger\hat{\sigma}_- + \hat{a}\hat{\sigma}_+)$, and $\hat{V}_{\rm nr} = \Omega_{\rm R}(\hat{a}^\dagger\hat{\sigma}_+ + \hat{a}\hat{\sigma}_-)$. The counter-rotating terms do not conserve the number of excitations. They can be neglected when $\Omega_{\rm R}/(\omega_{\rm c} + \omega_{eg}) \ll 1$. The interaction Hamiltonian has a structure which is very similar to that of the QED interaction potential, although it is less complicated. The quantum Rabi

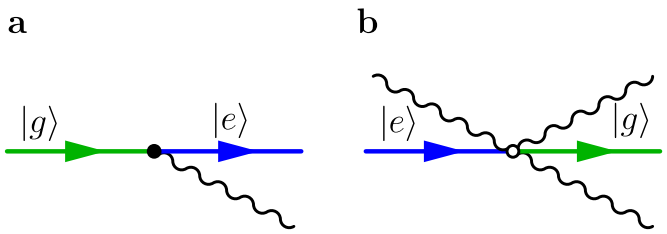

Figure 1. Diagrams for processes in the quantum Rabi model. The horizontal lines, coloured blue for $|e\rangle$ and green for $|g\rangle$, represent the qubit states and the wavy lines are the cavity photons. (a) Diagram for the transition $|g,\ 0\rangle \rightarrow |e,\ 1\rangle$, induced by the counter-rotating term $\hat{a}^\dagger\hat{\sigma}_+$. The filled vertex is used to mark counter-rotating processes. (b) Diagram for the transition $|e,\ 1\rangle \rightarrow |g,\ 2\rangle$. This is a resonant process, induced by the term $\hat{a}^\dagger\hat{\sigma}_-$, marked by an empty vertex. For a process with stimulated emission, such as this one, each photon involved is represented by a separate wavy line. This is the convention used in the rest of this article.

model can be viewed as a very simple QED system, where there is only a single photon mode and a two-state electron. As a consequence, we would expect that Feynman diagrams for the Rabi Hamiltonian will be a simplified version of QED diagrams. One such diagram, for the counter-rotating transition $|g,\ 0\rangle \rightarrow |e,\ 1\rangle$ (the second entry in the ket denotes the photon number), is shown in figure 1(a).

However, some care must be taken when drawing diagrams for processes involving more than one photon in the same mode [52], which occur in cavity QED. Stimulated emission [53], the mechanism behind laser action, is one such process. It is a one-photon process $|e,\ n\rangle \rightarrow |g,\ n+1\rangle$, where the n photons in the initial state stimulate the downward transition of the atom, affecting the transition rate which becomes proportional to $n+1$. This factor must be included in the rules for the diagrams in order for calculations to be correct. An example of a diagram showing the stimulated-emission process $|e,\ 1\rangle \rightarrow |g,\ 2\rangle$ is presented in figure 1(b). A more detailed discussion about diagrams for stimulated emission can be found in appendix A.

2.2. Bare versus physical excitations

Owing to the presence of $\hat{V}_{\rm nr}$ in the Rabi Hamiltonian, the operator describing the total number of excitations, $\hat{N} = \hat{a}^\dagger\hat{a} + |e\rangle\langle e|$, does not commute with $\hat{H}_{\rm R}$ and as a consequence the eigenstates of $\hat{H}_{\rm R}$ do not have a definite number of excitations [39]. When $\hat{V}_{\rm nr}$ can be neglected, the Hamiltonian becomes block-diagonal and easy to diagonalize (this is the Jaynes–Cummings (JC) model [54]). The resulting eigenstates can be labelled according to their definite number of excitations n. The ground state (zero excitations) is simply $|\mathcal{E}_0\rangle = |g,\ 0\rangle$, and the $n \geqslant 1$ excitation states $|\mathcal{E}_n^\pm\rangle$, obtained by diagonalization of 2×2 subspaces, can be written as

$$|\mathcal{E}_n^+\rangle = \mathcal{C}_n|g,\ n\rangle + \mathcal{S}_n|e,\ n-1\rangle \qquad |\mathcal{E}_n^-\rangle = -\mathcal{S}_n|g,\ n\rangle + \mathcal{C}_n|e,\ n-1\rangle, \tag{2}$$

where $\mathcal{C}_n$ and $\mathcal{S}_n$ are amplitudes determined by $\Omega_{\rm R}$ and the detuning $\omega_{\rm c} - \omega_{eg}$. The eigenstates $|E_i\rangle$ of the full Rabi Hamiltonian, however, are expressed as a superposition of bare states with varying numbers of bare excitations (see, e.g., [40]):

$$|E_i\rangle = \sum_{k=0}^{\infty}(c_{g,k}^i|g,\ k\rangle + d_{e,k}^i|e,\ k\rangle), \tag{3}$$

where the coefficients $c_{g,k}^i$ and $d_{e,k}^i$ are determined by $\Omega_{\rm R}$, $\omega_{\rm c}$ and ω_{eg}. When $\Omega_{\rm R} \ll \omega_{\rm c},\ \omega_{eg}$, the Rabi eigenstates reduce to the JC ones. Note that while $\hat{N}$ is not conserved with the Rabi Hamiltonian, the parity (even or odd number of excitations) still is [10, 55–57].

The mean photon number for the system in its ground state is

$$\langle E_0\ |\hat{a}^\dagger\hat{a}|\ E_0\rangle = \sum_k k(|c_{g,k}^0|^2 + |d_{e,k}^0|^2). \tag{4}$$

These ground-state photons cannot be detected yet. Otherwise the system, emitting a continuous stream of photons from its ground state, would be a perpetual-motion machine. However, the ground-state photons affect vacuum fluctuations (temporary random changes of the field amplitude) even if the field is in its lowest energy state. These fluctuations can be quantified considering the variance of a field quadrature, e.g., $\Delta x^2 = \langle\hat{x}^2\rangle - \langle\hat{x}\rangle^2$. For the empty cavity, or for the JC ground state, it is easy to find that $\Delta x^2 = 1$. For the ground state of the quantum Rabi model, $\Delta x^2 > 1$, owing to the additional contribution of the photon number states which are present in $|E_0\rangle$. Moreover, Δx^2 increases with increasing coupling strength $\Omega_{\rm R}$. Hence, we can conclude that the photons in $|E_0\rangle$, although not being observable in photon-counting experiments, contribute to vacuum fluctuations, which is a feature of virtual particles. The virtual nature of these photons is further shown in the next subsection.

As discussed in the introduction, the output emission rate from a single-mode resonator is proportional to $\langle\hat{x}^-\hat{x}^+\rangle$ [15, 40]. For weak coupling (or neglecting counter-rotating terms), $\langle\hat{a}^\dagger\hat{a}\rangle$ and $\langle\hat{x}^-\hat{x}^+\rangle$ coincide; but in the

Table 1. Bare and physical photonic correlation functions for the ground state of the JC model and for the four lowest-energy states of the quantum Rabi model. The table provides information on the number of real photons and on the existence of bare photons in these states. The last column shows the deviation of the ground-state variance from that of a noninteracting cavity mode. In the row for $|E_0\rangle$, we note that the nonzero expectation value for $\langle \hat{a}^{\dagger n}\hat{a}^n\rangle$ indicates that this state contains a nonzero number of bare photons. Moreover, this state displays no detectable photons ($\langle \hat{x}^{-n}\hat{x}^{+n}\rangle = 0$) together with a modification of the amplitude of vacuum fluctuations ($\langle \hat{x}^2\rangle - 1 \neq 0$); a clear indication that the bare photons are virtual particles.

State	$\langle \hat{a}^{\dagger n}\hat{a}^n\rangle$	$\langle \hat{x}^-\hat{x}^+\rangle$	$\langle \hat{x}^{-2}\hat{x}^{+2}\rangle$	$\langle \hat{x}^{-3}\hat{x}^{+3}\rangle$	$\langle \hat{x}^2\rangle - 1$
$\|\mathcal{E}_0\rangle$	$=0$	$=0$	$=0$	$=0$	$=0$
$\|E_0\rangle$	$\neq 0$	$=0$	$=0$	$=0$	$\neq 0$
$\|E_1\rangle$	$\neq 0$	$\neq 0$	$=0$	$=0$	—
$\|E_2\rangle$	$\neq 0$	$\neq 0$	$=0$	$=0$	—
$\|E_3\rangle$	$\neq 0$	$\neq 0$	$\neq 0$	$=0$	—

USC regime they can differ markedly. The components $\hat{x}^+$ and $\hat{x}^-$ are obtained in the eigenvector basis of $\hat{H}_{\rm R}$ as $\hat{x}^+ = \sum_{i<j} x_{ij}\ |E_i\rangle\langle E_j|$, where $x_{ij} = \langle E_i\ |\hat{x}|\ E_j\rangle$, if the eigenstates of $\hat{H}_{\rm R}$ are labelled according to their eigenvalues such that $E_k > E_j$ for $k > j$. As expected, we find that

$$\langle E_0\ |\hat{x}^-(t)\hat{x}^+(t)|\ E_0\rangle = 0,$$

which demonstrates that the photonic Fock states enriching the quantum Rabi ground state are actually virtual. This reasoning can be generalised to the excited states of the system. For the first excited state, the one-photon correlation is different from zero:

$$\langle E_1\ |\hat{x}^-(t)\hat{x}^+(t)|\ E_1\rangle \neq 0.$$

However, the output coincidence rate from this state, proportional to the *physical* two-photon correlation function $\langle E_1\ |(\hat{x}^-)^2(\hat{x}^+)^2|\ E_1\rangle$, is equal to zero. On the contrary, the correlation functions for $n \geqslant 2$ bare photons in the first excited state are different from zero; e.g.,

$$\langle E_1\ |(\hat{a}^\dagger)^2(\hat{a})^2|\ E_1\rangle \neq 0.$$

We can conclude that $|E_1\rangle$, like the corresponding JC eigenstate $|\mathcal{E}_1^-\rangle$, contains a single physical excitation. However, unlike the JC eigenstates, it is enriched by a larger number of virtual photons. In table 1 we summarise, for the JC ground state $|\mathcal{E}_0\rangle$ and for the lowest-energy states $|E_i\rangle$ ($i = 0,\ 1,\ 2,\ 3$) of the quantum Rabi model, when the nth-order photonic correlations (for bare and dressed photons) are zero or have finite values. Table 1 also shows that the field vacuum fluctuations are affected by the bare photons present in the ground state.

2.3. Energy corrections and loop diagrams

The analytical spectrum of $H_{\rm R}$ is defined in terms of the power series of a transcendental function [51]. Moreover, the eigenstates of the quantum Rabi model can be easily derived numerically with high accuracy. However, approximate forms, which can be derived by a perturbative approach (see, e.g., [58]), can provide more insight. Specifically, we will show below that a perturbative diagrammatic approach provides a direct visualisation of virtual and physical photons involved in the physical processes. Let us consider the correction to the ground state energy $\Delta_0 \equiv E_0 - \mathcal{E}_0$. The lowest nonzero-order (in the counter-rotating potential) contribution can be expressed as

$$\Delta_0^{(2)} = \langle g,\ 0\ |\hat{V}_{\rm nr}\hat{G}(\mathcal{E}_0)\hat{V}_{\rm nr}|\ g,\ 0\rangle, \tag{5}$$

where $\hat{G}(z) = (z - \hat{H}_0 - \hat{V}_{\rm r})^{-1}$ is the JC Green's function. The Green's function $\hat{G}(z)$ can be directly calculated by using the JC eigenstates from equation (2). Alternatively, it can be expressed in a Dyson series containing $\hat{V}_{\rm r}$ and the Green's function $\hat{G}_0(z) = (z - \hat{H}_0)^{-1}$ in the absence of interaction:
$\hat{G} = \hat{G}_0 + \hat{G}_0\hat{V}_{\rm r}\hat{G}_0 + \hat{G}_0\hat{V}_{\rm r}\hat{G}_0\hat{V}_{\rm r}\hat{G}_0 + \ldots$. Thus, equation (5) can be expanded as

$$\Delta_0^{(2)} = \langle g,\ 0\ |\hat{V}_{\rm nr}\hat{G}_0(\mathcal{E}_0)\hat{V}_{\rm nr}|\ g,\ 0\rangle + \langle g,\ 0\ |\hat{V}_{\rm nr}\hat{G}_0(\mathcal{E}_0)\hat{V}_{\rm r}\hat{G}_0(\mathcal{E}_0)\hat{V}_{\rm nr}|\ g,\ 0\rangle + \ldots. \tag{6}$$

A direct inspection of the terms in the series shows that only the terms with an even number of $V_{\rm r}$ are different from zero. It is possible to associate a diagram with each of the terms in the series appearing in equation (6). Figure 2(a) shows the first three diagrams providing a nonzero contribution. The first one corresponds to the first term on the rhs of equation (6). The second diagram describes the third term in the series:
$\langle g,\ 0\ |\hat{V}_{\rm nr}\hat{G}_0(\mathcal{E}_0)\hat{V}_{\rm r}\hat{G}_0(\mathcal{E}_0)\hat{V}_{\rm r}\hat{G}_0(\mathcal{E}_0)\hat{V}_{\rm nr}|\ g,\ 0\rangle$. Each bubble diagram, corresponding to a matrix element of $\hat{G}_0$, describes intermediate virtual excitations. This can be explicitly shown by inserting identity operators in each term of the series in equation (6). In this way, we obtain products involving only off-shell nonsingular

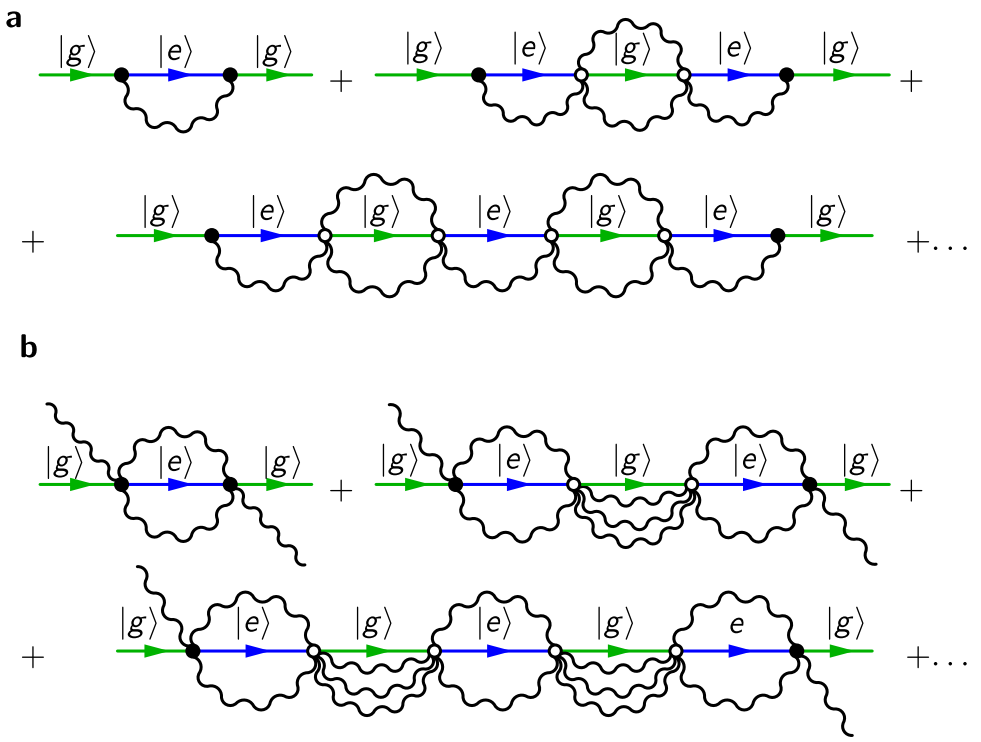

Figure 2. Feynman diagrams contributing to the energy correction of the ground state (a), and of the first excited state (b) of the Rabi Hamiltonian. Each bubble diagram, corresponding to a matrix element of $\hat{G}_0$, describes the intermediate virtual excitations enriching the ground and the first excited states. The virtual excitations originate from the counter-rotating terms in the interaction Hamiltonian.

propagators: $\langle g,\ 2\ |\hat{G}_0(\mathcal{E}_0)|\ g,\ 2\rangle$ and $\langle e,\ 1\ |\hat{G}_0(\mathcal{E}_0)|\ e,\ 1\rangle$ (see also appendix A). In QFT, virtual particles, corresponding to nonsingular internal propagators in the Feynman diagrams, are termed off-shell because they do not obey the energy–momentum relation. In our case, the virtual excitations induce a shift of the energy levels, in analogy with the Lamb shift in QED. The latter result originates from the interaction between an orbiting electron and the virtual particles in the surrounding vacuum. All the resulting bubble diagrams contain at most two photon waves, since we considered only the lowest nonzero-order corrections in the counter-rotating potential. Four and more photon waves arise when going beyond second-order perturbation theory in $\hat{V}_{\rm nr}$. As in QFT, physical particles are described by external (incoming or outgoing) lines in Feynman diagrams. The absence of external photon (wavy) lines in figure 2(a) confirms the absence of real particles in the ground state.

This approach can also be applied to the excited states. Considering the first excited state, we obtain

$$\Delta_1^{(2)} = \langle \mathcal{E}_1^+\ |\hat{V}_{\rm nr}\hat{G}(\mathcal{E}_1^+)\hat{V}_{\rm nr}|\ \mathcal{E}_1^+\rangle = \mathcal{C}_1^2\langle g,\ 1\ |\hat{V}_{\rm nr}\hat{G}(\mathcal{E}_1^+)\hat{V}_{\rm nr}|\ g,\ 1\rangle. \tag{7}$$

The mean value over the state $|g,\ 1\rangle$ in equation (7) can be expanded by exploiting the Dyson series. The corresponding first three diagrams providing a nonzero contribution are displayed in figure 2(b). Analogously to what was discussed above, the terms of the series contain only nonsingular internal propagators in the Feynman diagrams, in this case corresponding to the off-shell nonsingular propagators $\langle g,\ 3\ |\hat{G}_0(\mathcal{E}_1)|\ g,\ 3\rangle$ and $\langle e,\ 2\ |\hat{G}_0(\mathcal{E}_0)|\ e,\ 2\rangle$ (see appendix E). They are described by diagrams with internal loops where one or two additional virtual photons are created and finally reabsorbed. The Feynman diagrams in figure 2(b) display only one external photon line. This confirms that the first excited state contains only one physical photon. The energy corrections $\Delta_0^{(2)}$ and $\Delta_1^{(2)}$ can be easily evaluated by directly using $\hat{G}(z)$ or by summing up the infinite contributions arising from the Dyson series and described by the diagrams. These calculations, and a comparison between the approximate analytical energy corrections and the corresponding nonperturbative numerical calculations, can be found in appendix B. We observe that the analysis, carried out with the help of Feynman diagrams for the ground and the first excited states, provides a powerful tool to directly discern between real and virtual excitations in the eigenstates of the quantum Rabi Hamiltonian. Below we will show how this diagrammatic analysis also provides a clear picture of the conversion from virtual to real photons.

2.4. Three-level atom

We now consider a system consisting of a single-mode cavity interacting with the upper two levels $|e\rangle$ and $|g\rangle$ of a three-level atom [59, 60]. The energy difference E_{gs} between the middle level $|g\rangle$ and the bottom level $|s\rangle$ is

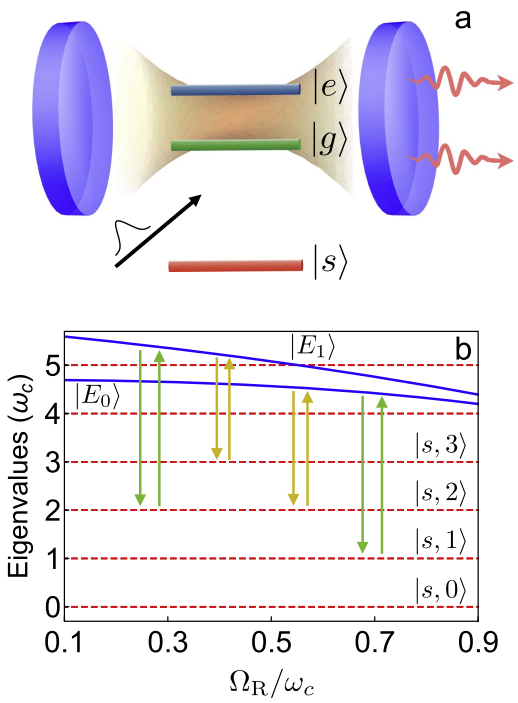

Figure 3. (a) Schematic of the system in which a three-level atom is placed in a cavity. The upper two levels $|e\rangle$ and $|g\rangle$ of the atom resonantly couple to a single cavity mode. The effective atom-cavity interaction can be controlled by external electromagnetic pulses (arrow with a Gaussian pulse) inducing transitions from the cavity-interacting levels $|g\rangle$ and $|e\rangle$ to the noninteracting level $|s\rangle$ and vice versa. These pulses can induce the emission of photons (red arrows) enriching the ground or the excited states of the Rabi Hamiltonian. (b) Lowest energy-levels of the system as a function of the normalised coupling strength Ω_R/ω_c and the transitions stimulated by the external pulses. Yellow arrows mark transitions induced by $\hat{V}_{sg}$ and green arrows mark transitions induced by $\hat{V}_{se}$.

assumed to be much larger than the cavity-mode resonance frequency such that the cavity does not interact significantly with the atom in the lowest energy state $|s\rangle$ (see figure 3(a)). The interaction of this transition with tha cavity can be further reduced considering three-level atoms with dipole moments μ_{sg}, $\mu_{se} \ll \mu_{ge}$. As we will show, the additional state $|s\rangle$ enables an effective on/off-switch of the atom-cavity interaction. The system Hamiltonian is simply $\hat{H}_C = \hat{H}_R + \omega_s\ |s\rangle\langle s|$. This Hamiltonian is block-diagonal and its eigenstates can be separated into a non-interacting sector $|s,\ n\rangle$, with energy $\omega_s + n\omega_c$, where n labels the cavity photon number, and dressed atom-cavity states $|E_i\rangle$, resulting from the diagonalization of the Rabi Hamiltonian (see figure 3(b)).

The direct excitation of the atom by applied electromagnetic pulses is described by the Hamiltonian

$$\hat{H}_d = \mathcal{E}_d(t)(\hat{V}_{sg} + \hat{V}_{se}), \tag{8}$$

where $\hat{V}_{sg} = \mu_{sg}(|g\rangle\langle s| + |s\rangle\langle g|)$, $\hat{V}_{se} = \mu_{se}(|e\rangle\langle s| + |s\rangle\langle e|)$, and μ_{sg} and μ_{se} are the dipole moments (here assumed to be real) for the transitions $|s\rangle \leftrightarrow |g\rangle$ and $|s\rangle \leftrightarrow |e\rangle$, respectively. We consider quasi-monochromatic pulses $\mathcal{E}_d(t) = A(t)\cos(\omega t)$, where $A(t)$ is a Gaussian envelope. We only consider pulses which are out of resonance with the transition $|g\rangle \leftrightarrow |e\rangle$ and neglect this transition in equation (8). If the system is prepared in a dressed state $|E_i\rangle$, the driving Hamiltonian $\hat{H}_d$ can induce transitions towards the noninteracting states $|s,\ m\rangle$:

$$\hat{H}_d|E_i\rangle = \mathcal{E}_d(t)\sum_{k=0}^{\infty}(\mu_{sg}c^i_{g,k}|s,\ k\rangle + \mu_{se}d^i_{e,k}|s,\ k\rangle). \tag{9}$$

Thus $\hat{H}_d$, when applied to a dressed state, is able to convert the virtual photons enriching the physical excitations into real ones which can be detected. This is possible because $\hat{H}_d$ induces transitions from the atomic states $|g\rangle$ and $|e\rangle$ (coupled to the cavity) to the noninteracting state $|s\rangle$. Of course, the transitions only occur if the driving-field frequency ω is resonant with the frequency of the corresponding transition $|E_i\rangle \rightarrow |s,\ m\rangle$. Note also that, if the artificial atom displays parity symmetry, only one of the two dipole moments (μ_{sg} and μ_{se}) will be nonzero. However, in artificial atoms (e.g., flux qubits), parity symmetry can be easily broken [61].

In the absence of counter-rotating terms, a JC eigenstate with n excitations can only undergo transitions towards states with n photons: $|E^{\pm}_n\rangle \rightarrow |s,\ n\rangle$ (for $\mu_{sg} \neq 0$), or $n-1$ photons: $|E^{\pm}_n\rangle \rightarrow |s,\ n-1\rangle$ (for $\mu_{se} \neq 0$).

2.5. Stimulated emission and reabsorption of virtual particles

We first consider the system prepared in the ground state $|E_0\rangle$ of the quantum Rabi Hamiltonian. This state can be easily reached from the ground state $|s\rangle$ by directly exciting the artificial atom with a resonant π-pulse [7]. As

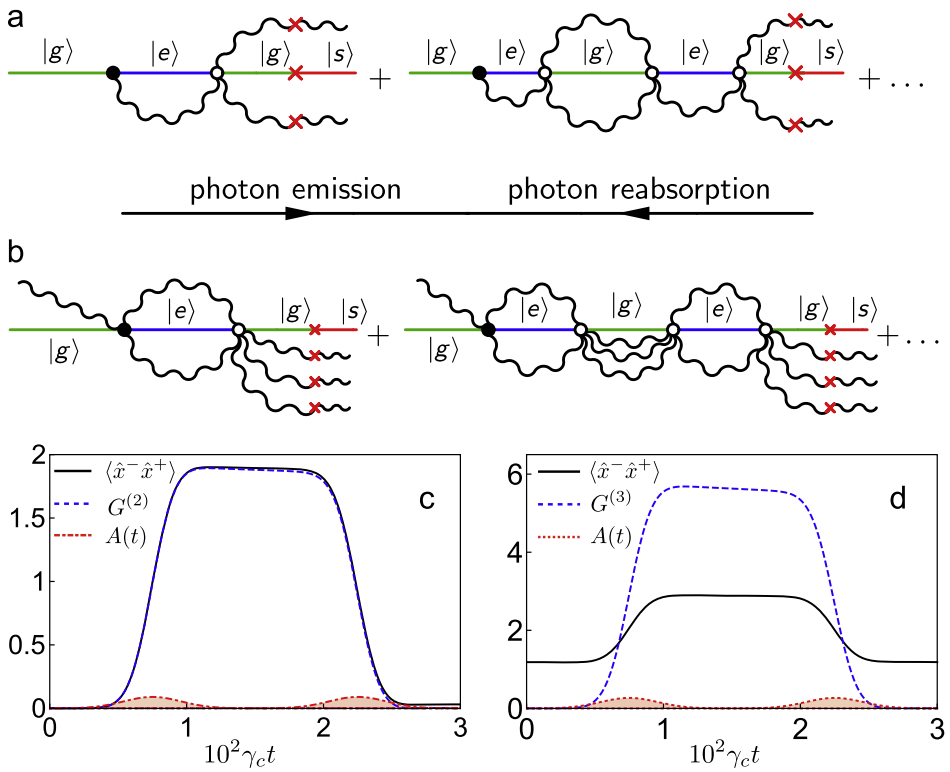

Figure 4. (a) Diagrams contributing to the transition matrix element $\langle s,\,2\,|\hat{V}_{sg}|\,E_0\rangle$, associated with the transition $|E_0\rangle \rightarrow |s,\,2\rangle$ (rightward time-arrow) where two cavity photons are emitted. The same diagrams but with a leftward time-arrow describe the reverse transition $|s,\,2\rangle \rightarrow |E_0\rangle$, where two cavity photons get trapped into the Rabi ground state. (b) Diagrams contributing to the matrix element $\langle s,\,3\,|\hat{V}_{sg}|\,E_1\rangle$, associated with the transitions $|E_1\rangle \leftrightarrow |s,\,3\rangle$, where three photons enriching the lowest-energy excited state of the Rabi Hamiltonian are emitted or reabsorbed back. The red crosses represent the perturbation $\hat{V}_{sg}$. (c) Numerical calculations of the mean cavity-photon number (continuous black curve), and of the two-photon correlation function (dashed blue curve) corresponding to diagrams in figure 4(a). The system is initially prepared in the state $|E_0\rangle$. A π pulse, resonantly exciting the system from $|E_0\rangle$ to $|s,\,2\rangle$, is then sent. A second (red) pulse induces the transition back from $|s,\,2\rangle$ to $|E_0\rangle$. (d) Numerical calculations of the mean cavity-photon number (continuous black curve), and of the three-photon correlation function (dashed blue curve) corresponding to diagrams in figure 4(b). The system is initially prepared in the state $|E_1\rangle$. A π pulse (filled curve), resonantly exciting the system from $|E_1\rangle$ to $|s,\,3\rangle$, is then sent. A second pulse induces the transition back from $|s,\,3\rangle$ to $|E_1\rangle$. Here we used $\Omega_R/\omega_c = 0.15$, $\omega_{eg} = \omega_c$, and $\gamma_{eg} = \gamma_{gs} = \gamma_c = 2 \times 10^{-5}\omega_c$, where γ_c is the decay rate for the cavity photons and γ_{eg}, γ_{gs} are the decay rates for the atom transitions $|e\rangle \rightarrow |g\rangle$ and $|g\rangle \rightarrow |s\rangle$.

long as the system remains in the state $|E_0\rangle$ (even if it is not the ground state of the total Hamiltonian $\hat{H}_R + \omega_s\,|s\rangle\langle s|$), no cavity photons can be observed, since the photons in $|E_0\rangle$ are virtual. An input pulse of central frequency $\omega \simeq E_0 - \omega_s - 2\omega_c$ can induce a transition $|E_0\rangle \rightarrow |s,\,2\rangle$, corresponding to a stimulated emission process (see figure 3(b)). The corresponding matrix element $\langle s,\,2\,|\hat{V}_{sg}|\,E_0\rangle = \mu_{sg}\,\langle g,\,2|E_0\rangle$, determining the transition probability, is proportional to the probability amplitude $c^0_{g,2} = \langle g,\,2|E_0\rangle$ that in the Rabi ground state there are two virtual photons. By exploiting perturbation theory (see appendix C), this matrix element can be approximated as $\langle s,\,2\,|\hat{V}_{sg}\hat{G}(\mathcal{E}_0)\hat{V}_{nr}|\,g,\,0\rangle$. From the Dyson series, we obtain

$$\langle s,\,2\,|\hat{V}_{sg}\hat{G}(\mathcal{E}_0)\hat{V}_{nr}|\,g,\,0\rangle = \langle s,\,2\,|\hat{V}_{sg}\hat{G}_0(\mathcal{E}_0)\hat{V}_{nr}|\,g,\,0\rangle + \langle s,\,2\,|\hat{V}_{sg}\hat{G}_0(\mathcal{E}_0)\hat{V}_r\hat{G}_0(\mathcal{E}_0)\hat{V}_{nr}|\,g,\,0\rangle + \langle s,\,2\,|\hat{V}_{sg}\hat{G}_0(\mathcal{E}_0)\hat{V}_r\hat{G}_0(\mathcal{E}_0)\hat{V}_r\hat{G}_0(\mathcal{E}_0)\hat{V}_{nr}|\,g,\,0\rangle + \ldots. \quad (10)$$

Figure 4(a) displays the diagrams describing the first nonzero terms in this series. The red crosses represent the action of the perturbation $\hat{V}_{sg}$. These Feynman diagrams provide a clear interpretation of the emission process. The loops in figure 2 contain virtual photons which contribute to the energy correction of the state $|E_0\rangle$ and $|E_1\rangle$. As shown in figure 4, the time-dependent perturbation $\hat{V}_{sg}$ is able to cut these loops. These diagrams show that the virtual photons in the loops are not just a technical feature of perturbation theory but describe internal physical processes, which can be interrupted by a suitable perturbation able to convert each virtual photon into an observable physical photon. Specifically, diagrams in figure 4(a) together with the rightward time-arrow describe the transition $|E_0\rangle \rightarrow |s,\,2\rangle$, where two cavity photons are emitted. The same diagrams, but with a leftward time-arrow, describe the transition $|s,\,2\rangle \rightarrow |E_0\rangle$, where two cavity photons are reabsorbed into the Rabi ground state. The potential $\hat{V}_{sg}$ induces the breaking of two-photon loops, converting virtual photon

pairs into real ones. It is not able, however, to break one-photon loops. These can be broken by the potential $\hat{V}_{se}$ as shown below.

It is even more interesting to undress the excited states of the quantum Rabi model. This can provide access to the relationship between bare and physical excitations. Let us consider the lowest-energy excited state $|E_1\rangle$ which, as we have shown in section 2.2, is a single-particle state. Following the same steps as used in obtaining the series in equation (10), the diagrams in figure 4(b) can be drawn. According to the Fermi golden rule, an input pulse of central frequency $\omega \simeq E_1 - \omega_s - 3\omega_c$ can induce a transition $|E_1\rangle \rightarrow |s,\ 3\rangle$. The corresponding matrix element $\langle s,\ 3\ |\hat{V}_{sg}|\ E_1\rangle = \mu_{sg} c^1_{g,3}$ is proportional to the probability amplitude that in the state $|E_1\rangle$ there are three bare photons. By applying perturbation theory, it can be approximated as (see appendix C)

$$\langle s,\ 3\ |\hat{V}_{sg}|\ E_1\rangle = -\mathcal{S}_1 \langle s,\ 3\ |\hat{V}_{sg}\hat{G}(\mathcal{E}_1^-)\hat{V}_{\rm nr}|\ g,\ 1\rangle. \tag{11}$$

The analytical perturbative calculations of the matrix elements $\langle s,\ 2\ |\hat{V}_{sg}|\ E_0\rangle$ and $\langle s,\ 3\ |\hat{V}_{sg}|\ E_1\rangle$ are described in appendix C.

We complete the above analysis by presenting nonperturbative numerical calculations which accurately describe the dynamics of the undressing and re-dressing of the Rabi vacuum and of the Rabi lowest-energy excitation.

The spectrum and the eigenstates of the quantum Rabi Hamiltonian $\hat{H}_{\rm R}$ have been obtained by standard numerical diagonalization in a truncated finite-dimensional Hilbert space. The truncation is realised by including only the N lowest-energy Fock states for the cavity mode. The truncation number N is chosen in order to ensure that the lowest M energy eigenvalues and corresponding eigenvectors, which are involved in the dynamical processes investigated here, are not affected significantly when increasing N. These results have been obtained using $N = 30$, although numerical stability can also be achieved with a lower N.

We take into account the presence of dissipation channels, the presence of higher energy levels in the Rabi Hamiltonian, and the non-monochromaticity of the driving pulses. All the dynamical evolutions displayed in figures 4(c) and (d) have been calculated numerically solving the master equation $\dot{\hat{\rho}}(t) = {\rm i}[\hat{\rho}(t),\ \hat{H}_{\rm C}] + \sum_j \hat{\mathcal{L}}_j \hat{\rho}(t)$ [40, 62, 63], where $\hat{\mathcal{L}}_j$ are Liouvillian superoperators describing the different (atomic and photonic) dissipation channels. All calculations have been carried out with zero-temperature reservoirs, which is a reasonable assumption for systems at very low temperatures. For instance, for a system with a resonator at frequency $\omega_c/(2\pi) = 10$ GHz and temperature $T = 40$ mK, the number of thermal photons is lower than 10^{-5}. All the numerical calculations have been performed using $\gamma_{eg} = \gamma_{gs} = \gamma_c = 2 \times 10^{-5}\omega_c$, where γ_c is the decay rate for the cavity photons and γ_{eg}, γ_{gs} are the decay rates for the atomic transitions $|e\rangle \rightarrow |g\rangle$ and $|g\rangle \rightarrow |s\rangle$. These small decay rates are still shorter than the typical decay rates experimentally observed in state-of-the-art circuit QED systems (e.g., [64]). The density matrix, expressed in the basis of the system eigenstates, is truncated in order to exclude all the higher-energy eigenstates which are not populated during the dynamical evolution. The system of differential equations resulting from the master equation is solved by using a standard Runge–Kutta method with step control.

We consider the system initially prepared in the state $|E_0\rangle$ (preparation starting from the ground state $|s,\ 0\rangle$ can be easily achieved by sending a suitable π pulse). Then, a Gaussian pulse with central frequency $\omega = E_0 - \omega_s - 2\omega_c$ induces the transition $|E_0\rangle \rightarrow |s,\ 2\rangle$. Specifically, the pulse area required to obtain a complete transition is $\pi/|\langle s,\ 2\ |\hat{V}_{sg}|\ E_0\rangle|$. The pulse arrival-time corresponds to the time when the loops in the Feynman diagrams are cut. Figure 4(c) displays the dynamics of the intracavity mean excitation number $\langle \hat{x}^-\hat{x}^+\rangle$, which is directly related to the output photon flux $\Phi_{\rm out}(t) = \gamma_c \langle \hat{x}^-(t)\hat{x}^+(t)\rangle$ (where γ_c is the photon escape rate through the cavity boundary), as well as the equal-time second-order correlation function $G^{(2)}(t) = \langle (\hat{x}^-(t))^2(\hat{x}^+(t))^2\rangle$ [15]. Before the arrival of the Gaussian pulse (shaded red curve), the output photon flux is zero, since $\langle E_0\ |\hat{x}^-\hat{x}^+|\ E_0\rangle = 0$. After the arrival of the pulse, the photon flux becomes nonzero and $G^{(2)}(t) \simeq \langle \hat{x}^-\hat{x}^+\rangle$, confirming that a two-photon state is actually generated as expected from the diagrams in figure 4(a). When a second pulse is sent, the two photons are reabsorbed almost completely into the Rabi ground state: $|s,\ 2\rangle \rightarrow |E_0\rangle$ (diagrams in figure 4(a) with the leftward time-arrow). Figure 4(c) shows that a residual small excitation remains in the system after the arrival of the second pulse. This can be attributed to the influence of cavity losses which give rise to a spontaneous transition $|s,\ 2\rangle \rightarrow |s,\ 1\rangle$. As a result, a small but finite population in $|s,\ 1\rangle$ leads to $\langle \hat{x}^-\hat{x}^+\rangle \neq 0$ with $G^{(2)} = 0$. As expected, this residual excitation disappears in absence of dissipation.

Figure 4(d) displays the dynamics starting from the system prepared in the state $|E_1\rangle$. If the dipole moment $\mu_{es} \neq 0$, this state can be reached directly from the ground state $|s,\ 0\rangle$ by exciting the artificial atom with a resonant π-pulse. If $\mu_{es} = 0$, it is possible to reach the state in two steps ($|s,\ 0\rangle \rightarrow |E_0\rangle \rightarrow |E_1\rangle$). We observe that, after the arrival of the Gaussian pulse (with central frequency $\omega = E_1 - \omega_s - 3\omega_c$, and area $\pi/|\langle s,\ 3\ |\hat{V}_{sg}|\ E_1\rangle|$), the initially zero third-order correlation function $G^{(3)}$ approaches 6, the value corresponding to a three-photon state. This result confirms the occurrence of the transition $|E_1\rangle \rightarrow |s,\ 3\rangle$. Also in this case, the emitted photons

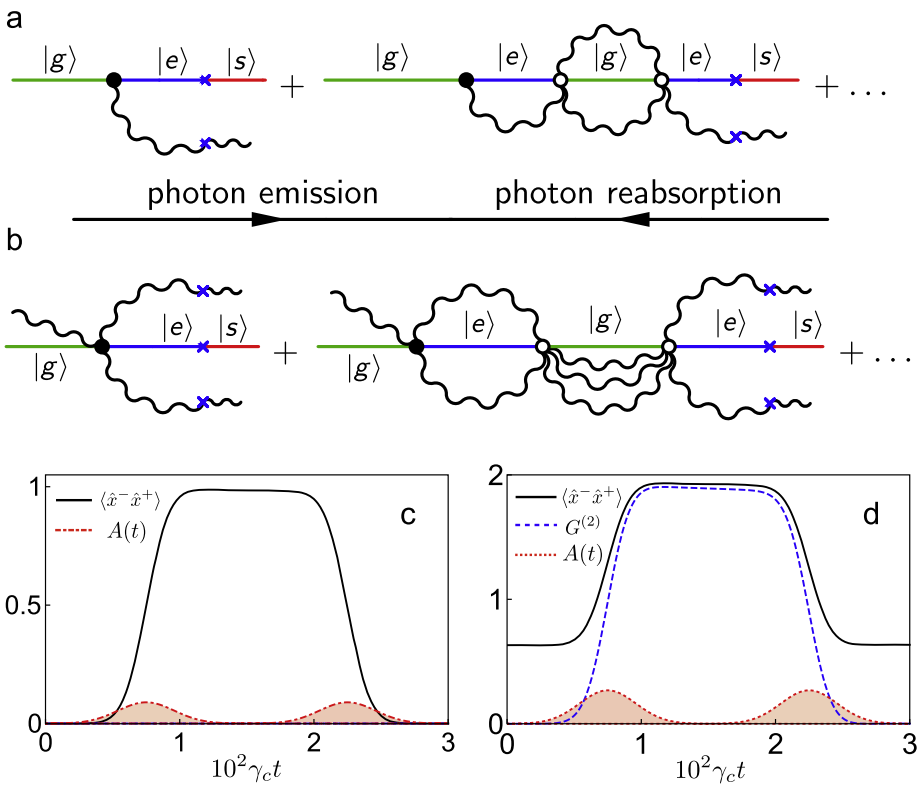

Figure 5. (a) Diagrams contributing to the matrix element $\langle s,\ 1\ |\hat{V}_{se}|\ E_0\rangle$, associated with the transition $|E_0\rangle \rightarrow |s,\ 1\rangle$ (rightward time-arrow) where a cavity photon is emitted. The same diagrams but with a leftward time-arrow describe the reverse transition $|s,\ 1\rangle \rightarrow |E_0\rangle$, where a cavity photon is absorbed into the Rabi ground state. (b) Diagrams contributing to the matrix element $\langle s,\ 2\ |\hat{V}_{se}|\ E_1\rangle$, associated with the transitions $|E_1\rangle \leftrightarrow |s,\ 2\rangle$, where two photons enriching the lowest-energy excited state $|E_1\rangle$ of the Rabi Hamiltonian are emitted or reabsorbed back. The blue crosses represent the perturbation $\hat{V}_{se}$. (c) Numerical calculations of the mean cavity-photon number (continuous black curve) corresponding to diagrams in figure 5(a). The system is initially prepared in the state $|E_0\rangle$. A π pulse (shown in red), resonantly exciting the system from $|E_0\rangle$ to $|s,\ 1\rangle$, is then sent. A second pulse induces the transition back from $|s,\ 1\rangle$ to $|E_0\rangle$. (d) Numerical calculations of the mean cavity-photon number (continuous black curve), and of the three-photon correlation function (dashed blue curve) corresponding to diagrams in figure 5(b). The system is initially prepared in the state $|E_1\rangle$. A π pulse (red filled curve), resonantly exciting the system from $|E_1\rangle$ to $|s,\ 2\rangle$, is then sent. A second pulse induces the transition back from $|s,\ 2\rangle$ to $|E_1\rangle$. For the other parameters of the simulation not specified here, the same values as in figure 4 were used.

are reabsorbed by sending an additional identical Gaussian pulse. We observe that, within the standard RWA, $\langle \mathcal{E}_1^+\ |\hat{x}^-(t)\hat{x}^+(t)|\ \mathcal{E}_1^+\rangle = 0.5$. Figure 4(d) at $t = 0$ displays a higher value. This is a peculiar effect of the USC regime, where the intracavity mean excitation number is quadrature-dependent. In particular, it increases for $\hat{x}$ measurements and decreases for measurements of the conjugate quadrature $\hat{y} = \mathrm{i}(\hat{a}^\dagger - \hat{a})$.

Having studied the above processes induced by $\hat{V}_{sg}$, we now turn to those involving $\hat{V}_{se}$ instead. Specifically, we consider the case where the dipole transition moment μ_{se} is different from zero. Figure 5 shows these processes, with the action of $\hat{V}_{se}$ represented in the diagrams by blue crosses. These processes are able to break one-photon loops, as illustrated in figure 5(a), which shows the diagrams associated with the transition $|E_0\rangle \rightarrow |s,\ 1\rangle$, where a cavity photon is emitted (rightward time-arrow) and reabsorbed (leftward time-arrow). Figure 5(b) shows the diagrams associated with the transitions $|E_1\rangle \leftrightarrow |s,\ 2\rangle$, where two photons enriching the lowest-energy excited state $|E_1\rangle$ of the Rabi Hamiltonian are emitted or reabsorbed. The analytical perturbative calculations of the matrix elements $\langle s,\ 1\ |\hat{V}_{se}|\ E_0\rangle$ and $\langle s,\ 2\ |\hat{V}_{se}|\ E_1\rangle$ are described in appendix D. In complete analogy with what was shown in figures 4(c) and (d), we present in figures 5(c) and (d) nonperturbative numerical calculations describing the dynamics of the undressing and re-dressing of the quantum Rabi vacuum and of the quantum Rabi lowest-energy excitation, taking into account the presence of dissipation channels, the presence of higher-energy levels, and the non-monochromaticity of the driving pulses. We first consider the system starting in the state $|E_0\rangle$, corresponding to an intracavity mean excitation number $\langle \hat{x}^-\hat{x}^+\rangle = 0$. Then, a Gaussian pulse with central frequency $\omega = E_0 - \omega_s - \omega_c$ induces a transition $|E_0\rangle \rightarrow |s,\ 1\rangle$. Specifically, the pulse area required to obtain a complete transition is $\pi/|\langle s,\ 1\ |\hat{V}_{se}|\ E_0\rangle|$. The pulse arrival-time corresponds to the time when the loops in the Feynman diagrams are cut. Figure 5(c) displays the time evolution of $\langle \hat{x}^-\hat{x}^+\rangle$.

After the arrival of the first pulse, $\langle \hat{x}^{-}\hat{x}^{+}\rangle$ jumps and almost reaches the value 1. The equal-time second-order correlation function $G^{(2)}(t)$, not displayed, remains zero, confirming that a single-photon state is generated.

Figure 5(d) displays the dynamics starting from the system prepared in the state $|E_1\rangle$. We observe that, after the arrival of the Gaussian pulse (with central frequency $\omega = E_1 - \omega_s - 2\omega_c$ and area $\pi/|\langle s,\ 2\ |\hat{V}_{se}|\ E_1\rangle|$), the initially zero second-order correlation function $G^{(2)}$ approaches 2, the value corresponding to a two-photon state. This result confirms the occurrence of the transition $|E_1\rangle \rightarrow |s,\ 2\rangle$. Also in this case, the emitted photons are reabsorbed after an additional identical Gaussian pulse is sent.

We observe that both in figures 4 and 5, a normalised coupling strength $\Omega_R/\omega_c = 0.15$ is sufficient to break one-, two-, and three-photon loops, converting virtual photons into real ones with probability close to one. This value of the normalised coupling strength is Ω_R/ω_c roughly equal to the experimentally demonstrated values in circuit-QED systems [24]. We note that $c^0_{e,1}$ and $c^1_{e,2}$ are significantly larger than $c^0_{g,2}$ and $c^1_{g,3}$, respectively. Hence the process induced by $\hat{V}_{se}$ can be observed even for smaller coupling strenghts.

3. Discussion

The results presented here show that the USC regime of cavity QED can be used to observe, in a direct way, how interactions dress the observable particles by a cloud of virtual particles. Such particle dressing is a general feature of QFT and many-body quantum systems. We have shown that, by applying external electromagnetic pulses of suitable amplitude and frequency, each virtual photon enriching a physical excitation can be converted into a physical observable photon. In this way, the hidden relationship between the bare and physical excitations can be unravelled and becomes experimentally testable. Virtual particles are represented by internal loops in Feynman diagrams. These loop or bubble diagrams describe internal processes where virtual photons are created and reabsorbed. The diagrams representing the conversion of virtual photons, dressing a physical excitation, into real ones can be obtained by cutting the loop diagrams describing energy corrections and taking the first half. Moreover, the stimulated reabsorption of real photons into the physical excitation, converting them to virtual photons, corresponds to the second half of the loop diagrams.

We limited our analysis to the dressed vacuum and to a one-particle state. It can be easily extended to study higher-energy excitations. Moreover, we considered only processes up to second-order perturbation theory in the counter-rotating potential $\hat{V}_{nr}$. The present analysis can be generalised to describe higher-order processes, involving more than three photons, which can take place if the light–matter interaction is sufficiently strong [35].

The most promising candidates for an experimental realisation of the proposed stimulated conversion effects are superconducting quantum circuits [65] and intersubband quantum-well polaritons. In particular, phase-biased flux qubits can reach the USC regime in circuit QED [66], as has been shown in experiments [23, 24, 35, 67]. Very recently, hybrid quantum circuits [68] with Ω_R/ω_{eg} ranging from 0.72 to 1.34 have been realised [35] by making use of the macroscopic magnetic dipole moment of a flux qubit, large zero-point-fluctuation current of an LC oscillator, and large Josephson inductance of a coupler junction. In flux qubits, an externally applied magnetic flux can be changed such that these artificial atoms acquire both the quantised level structure and the transition matrix elements required for the observation of the stimulated emission and reabsorption of virtual particles [7]. Specifically, the supplementary material of [7] contains a section where numerical calculations show how an artificial atom (a flux qubit) with a specific flux offset can provide the required level spacing and dipole moments to observe the effect. We have checked that working far from the sweet spot (around zero flux-offset) does not affect the results significantly. In addition, we observe that it is not necessary that level $|s\rangle$ has lower energy than $|g\rangle$. In this case, the standard configuration of flux qubits near the sweet spot can provide the required level structure and dipole moments [23, 24, 35]. The description of the stimulated emission and reabsorption of virtual photons presented here also holds if $|s\rangle$ has higher energy than the $|g\rangle$ and $|e\rangle$ states.

The USC regime can also be reached for intersubband transitions in undoped quantum wells [69]. In this system, an optical resonator in the terahertz spectral range is resonantly coupled to transitions between the two-lowest energy conduction subbands of a large number of identical undoped quantum wells. In this case, the upper valence subband plays the role of the lowest energy state $|s\rangle$ (see figure 3). Ultrafast optical pulses can induce transitions between the valence and conduction subbands prompting the conversion from virtual to real photons and vice versa.

Such experiments would provide deep insight into fundamental aspects of interaction processes in QFT and quantum many-body systems. They would pave the route for quantum emulation [70, 71] of fundamental processes in QED.

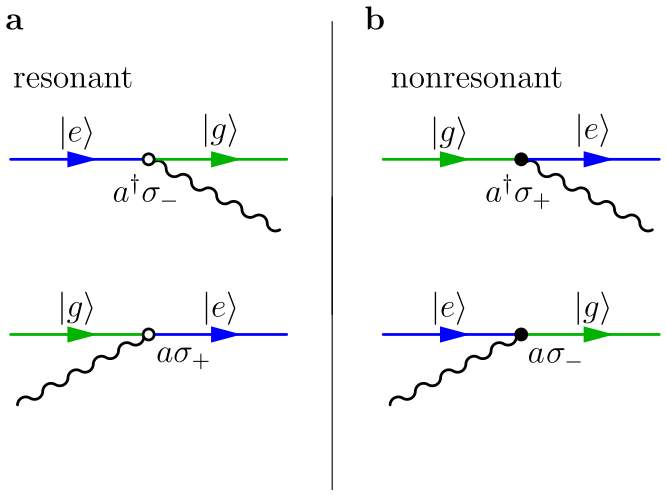

Figure A1. Diagrams corresponding to the four terms in the interaction Hamiltonian of the quantum Rabi model. The horizontal lines represent the qubit states and the wavy lines the cavity photons. (a) Diagrams corresponding to those terms in the interaction Hamiltonian that conserve energy when $\omega_c = \omega_{eg}$. (b) Diagrams for the terms $\propto \hat{a}^\dagger\hat{\sigma}_+$ and $\hat{a}\hat{\sigma}_-$, which conserve neither energy nor the number of excitations. Their elimination corresponds to the RWA.

Acknowledgments

FN was partially supported by the RIKEN iTHES Project, MURI Center for Dynamic Magneto-Optics via the AFOSR Award No. FA9550-14-1-0040, the Japan Society for the Promotion of Science (KAKENHI), the IMPACT program of JST, CREST grant No. JPMJCR1676, and the John Templeton Foundation. AFK acknowledges support from a JSPS Postdoctoral Fellowship for Overseas Researchers.

Appendix

In these appendix sections, we first restate some properties of the quantum Rabi model and its diagrammatic representation, expanding on the discussion in the main text. We then proceed to explicitly calculate analytically the second-order correction to the lowest energy eigenvalues and comparing them to full numerical calculations. We also calculate matrix elements associated with the external drive used to stimulate the emission and reabsorption of the virtual particles dressing the excitations in the system.

Appendix A. Hamiltonian and basic diagrams

The interaction Hamiltonian of the quantum Rabi model is

$$\hat{V} = \Omega_R(\hat{a}^\dagger + \hat{a})\hat{\sigma}_x, \tag{A1}$$

where Ω_R is the coupling strength and $\hat{\sigma}_x = \hat{\sigma}_+ + \hat{\sigma}_- = |e\rangle\langle g| + |g\rangle\langle e|$. Referring to the case $\omega_c \approx \omega_{eg} \equiv \omega_e - \omega_g$, the interaction Hamiltonian can be separated into a resonant and a nonresonant contribution: $\hat{V} = \hat{V}_r + \hat{V}_{nr}$, where $\hat{V}_r = \Omega_R(\hat{a}^\dagger\hat{\sigma}_- + \hat{a}\hat{\sigma}_+)$, and $\hat{V}_{nr} = \Omega_R(\hat{a}^\dagger\hat{\sigma}_+ + \hat{a}\hat{\sigma}_-)$. This interaction term has a structure which is very similar to that of the QED interaction potential, although it is simpler. The quantum Rabi model can be viewed as a prototypical QED system where there is only one photon mode and a two-state electron. Therefore, we expect that the Feynman diagrams for the Rabi Hamiltonian will be a simplified version of the QED diagrams.

As in QED, there is only one vertex type with three lines: one wavy (photonic) line, one solid line with an incoming arrow, and one solid line with an outgoing arrow. The vertices (of the same type) corresponding to the four terms in the interaction Hamiltonian are displayed in figure A1. The upper diagram in figure A1(a) describes the spontaneous emission process and the lower one the absorption process. Starting from these four building blocks, it is possible to describe higher-order processes as in QED. However, in cavity QED there are processes that are not described in a complete way by Feynman diagrams directly derived from this form of the interaction Hamiltonian. Specifically, the presence of a resonator supporting discrete modes opens up the possibility of observing processes involving more than one photon in the same mode. Stimulated emission, the process underlying laser action, is one of these. It is a one-photon process $|e, n\rangle \rightarrow |g, n+1\rangle$, where, however, the n photons in the initial state stimulate the downward transition of the atom, affecting the transition rate

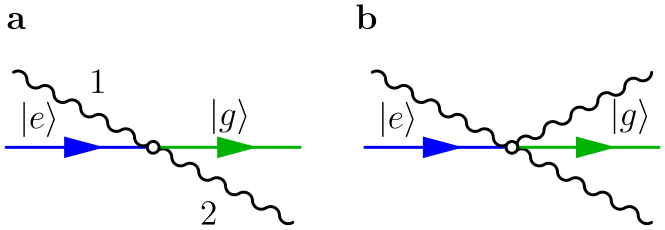

Figure A2. Diagrams corresponding to the the transition $|e,\ 1\rangle \rightarrow |g,\ 2\rangle$. (a) Diagram with one incoming and one outcoming wavy line, each labelled respectively with the number of photons involved in the process. (b) Diagram for the same process, but in this case each wavy line represents one single photon.

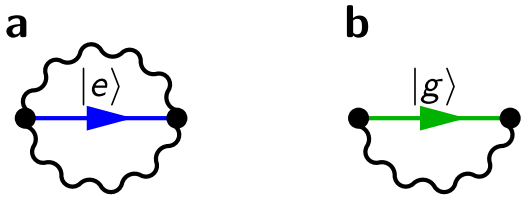

Figure A3. Examples of diagrams corresponding to the Green's function. (a) Diagram for $\langle e,\ 2\ |\hat{G}_0|\ e,\ 2\rangle$. (b) Diagram for $\langle g,\ 1\ |\hat{G}_0|\ g,\ 1\rangle$.

which becomes proportional to $n+1$. The Feynman diagram describing the process is the same one describing spontaneous emission ($n=0$), shown in figure A1(a). However, the transition rate for stimulated emission is $n+1$ times larger than that of spontaneous emission. Hence the Feynman diagram in the absence of additional rules is not able to uniquely determine the transition amplitude for this process.

A possible solution is to expand the photon creation and destruction operators in equation (A1) in the Fock basis. The resulting interaction operator is

$$\hat{V} = \Omega_{\mathrm{R}} \sum_{n=0}^{\infty} (\hat{\alpha}_{+}^{(n)} + \hat{\alpha}_{-}^{(n)})(\hat{\sigma}_{+} + \hat{\sigma}_{-}), \tag{A2}$$

where $\hat{\alpha}_{+}^{(n)} = \hat{a}^{\dagger}\ |n\rangle\langle n| = \sqrt{n+1}\ |n+1\rangle\langle n|$, and $\hat{\alpha}_{-}^{(n)} = \hat{a}\ |n\rangle\langle n| = \sqrt{n}\ |n-1\rangle\langle n|$ (notice that $\hat{\alpha}_{-}^{(0)} = 0$). This form of the interaction Hamiltonian consists of a sum of products of (upward or downward) atomic and photonic transition operators; thus photonic and atomic transitions are treated on an equal footing. In this case, each vertex is associated to two transition operators. For example, the vertex describing the transition $|e,\ 1\rangle \rightarrow |g,\ 2\rangle$ is shown in figure A2(a): the wavy lines describe the incoming and the outgoing photon states, while the continuous line with the arrows describes the incoming and outgoing electronic states. The vertex in figure A2(a) describes a stimulated emission process. Since the photon wavy lines are labelled by the photon number, an alternative (perhaps more visual) way to draw diagrams is to drop the photon label and draw a wavy line for each incoming or outgoing photon line as shown in figure A2(b). In this case, the vertices will have $n_{\mathrm{in}} = n$ incoming and $n_{\mathrm{out}} = n \pm 1$ outgoing wavy lines. Each vertex (full/empty circle) contributes with a factor $\sqrt{n}\ |\hat{V}_{\mathrm{r/nr}}|$, where $n = \max(n_{\mathrm{in}},\ n_{\mathrm{out}})$.

The Green's function for the system in the absence of interaction,

$$\hat{G}_{q}^{(n)}(z) \equiv \langle q,\ n\ |\hat{G}_0|\ q,\ n\rangle = \frac{1}{z - (\omega_{qg} + n\omega_{\mathrm{c}})}, \tag{A3}$$

where $\omega_{qg} = \omega_q - \omega_g$, with $q = e,\ g$, corresponds to a loop diagram with n wavy lines and one straight arrow. In figure A3, we show the two loop diagrams corresponding to $G_e^{(2)}$ and $G_g^{(1)}$.

Appendix B. Second-order correction to the energy eigenvalues

The well-known second-order correction to the nth energy eigenvalue is

$$\Delta E_n^{(2)} = \sum_{k}{}' \frac{|\langle E_k\ |\hat{V}|\ E_n\rangle|^2}{E_n^0 - E_k^0}, \tag{B1}$$

where the prime in the summation means that the values $k = n$ have to be excluded. For the first-order correction to the eigenfunction we have

$$|E_n^{(1)}\rangle = \sum_k{}' \frac{\langle E_k\,|\hat{V}|\,E_n\rangle}{E_n^0 - E_k^0}|E_k\rangle. \tag{B2}$$

Following [58], defining the projection operator onto the space orthogonal to $|n\rangle$, $\hat{Q}_n = \hat{1} - |n\rangle\langle n|$, equation (B2) becomes

$$|E_n^{(1)}\rangle = \hat{Q}_n\hat{G}(E_n^0)\hat{Q}_n\hat{V}|E_n\rangle, \tag{B3}$$

where

$$\hat{G}_0(E_n^0) = \frac{1}{E_n^0 - \hat{H}_0} \tag{B4}$$

is the unperturbed Green's function calculated for E_n^0, the unperturbed eigenenergy of the system.

Using the definition of the Green's function from equation (B4) and the projection operators, equation (B1) becomes

$$\Delta E_n^{(2)} = \langle E_k\,|\hat{V}\hat{Q}_n\hat{G}(E_n)\hat{Q}_n\hat{V}|\,E_n\rangle. \tag{B5}$$

We apply these results to the JC Hamiltonian perturbed by the non-resonant potential $\hat{V}_{\rm nr}$. In this case, the unperturbed Hamiltonian $\hat{H}_0$ becomes $\hat{H}_{\rm JC} = \hat{H}_0 + \hat{V}_{\rm r}$, whose eigenvalues and eigenstates are $\mathcal{E}_n^{\pm}$ and $|\mathcal{E}_n^{\pm}\rangle$, respectively. We have

$$|\mathcal{E}_n^{+}\rangle = \mathcal{C}_n|g,\,n\rangle + \mathcal{S}_n|e,\,n-1\rangle \qquad |\mathcal{E}_n^{-}\rangle = -\mathcal{S}_n|g,\,n\rangle + \mathcal{C}_n|e,\,n-1\rangle. \tag{B6}$$

The action of the non-resonant potential on these eigenstates is

$$\hat{V}_{\rm nr}|\mathcal{E}_n^{+}\rangle = \Omega_{\rm R}(\mathcal{C}_n|e,\,n+1\rangle + \mathcal{S}_n|g,\,n-2\rangle) \tag{B7}$$

and

$$\hat{V}_{\rm nr}|\mathcal{E}_n^{-}\rangle = \Omega_{\rm R}(-\mathcal{S}_n|e,\,n+1\rangle + \mathcal{C}_n|g,\,n-2\rangle). \tag{B8}$$

From the last two equations, we deduce that the non-resonant potential $\hat{V}_{\rm nr}$ determines transitions from the subspace n (spanned by $\mathcal{E}_n^{\pm}$) to $(n+2)$ or $(n-2)$ subspaces. As a consequence, we have

$$\hat{Q}_n\hat{V}_{\rm nr}|\mathcal{E}_n^{\pm}\rangle = \hat{V}_{\rm nr}|\mathcal{E}_n^{\pm}\rangle. \tag{B9}$$

Owing to this property, equation (B5) becomes

$$\Delta^{\pm(2)} = \Delta\mathcal{E}_n^{\pm(2)} = \langle\mathcal{E}_n^{\pm}\,|\hat{V}_{\rm nr}\hat{G}(\mathcal{E}_n^{\pm})\hat{V}_{\rm nr}|\,\mathcal{E}_n^{\pm}\rangle, \tag{B10}$$

where

$$\hat{G}(\mathcal{E}_n^{\pm}) = (\mathcal{E}_n^{\pm} - \hat{H}_{\rm JC})^{-1} = (\mathcal{E}_n^{\pm} - \hat{H}_0 - \hat{V}_{\rm r})^{-1} \tag{B11}$$

is the JC Green's function. Equation (B10) can be easily calculated exploiting the matrix elements of the JC Green's function by using the JC eigenstates. We do not follow this procedure because our scope is to show, through a diagrammatic analysis, the structure of the virtual processes that contribute to such a correction. For this purpose, we exploit the Dyson equation for the JC Green's function, considering now the resonant potential $\hat{V}_{\rm r}$ as the perturbation, and the Green's function in the absence of interaction $\hat{G}_0(\mathcal{E}_n) = (\mathcal{E}_n - H_0)^{-1}$: $\hat{G} = \hat{G}_0 + \hat{G}_0\hat{V}_{\rm r}\hat{G}_0 + \ldots$. Equation (B10) can thus be expanded as

$$\Delta_n^{\pm(2)} = \langle\mathcal{E}_n^{\pm}\,|\hat{V}_{\rm nr}\hat{G}_0(\mathcal{E}_n^{\pm})\hat{V}_{\rm nr}|\,\mathcal{E}_n^{\pm}\rangle + \langle\mathcal{E}_n^{\pm}\,|\hat{V}_{\rm nr}\hat{G}_0(\mathcal{E}_n^{\pm})\hat{V}_{\rm r}\hat{G}_0(\mathcal{E}_n^{\pm})\hat{V}_{\rm nr}|\,\mathcal{E}_n^{\pm}\rangle + \ldots. \tag{B12}$$

Using equation (B12), the lowest-order (second-order) correction to the ground state $|g,\,0\rangle$ energy due to the non-resonant potential $\hat{V}_{\rm nr}$ can be expressed as

$$\Delta_0^{(2)} = \langle g,\,0\,|\hat{V}_{\rm nr}\hat{G}(E_0)\hat{V}_{\rm nr}|\,g,\,0\rangle = \langle g,\,0\,|\hat{V}_{\rm nr}\hat{G}_0\hat{V}_{\rm nr}|\,g,\,0\rangle + \langle g,\,0\,|\hat{V}_{\rm nr}\hat{G}_0\hat{V}_{\rm r}\hat{G}_0\hat{V}_{\rm nr}|\,g,\,0\rangle + \ldots. \tag{B13}$$

By using the identity operator and exploiting the explicit expression of $\hat{V}_{\rm nr}$, equation (B13) can be expressed as

$$\Delta_0^{(2)} = \langle g,\,0\,|\hat{V}_{\rm nr}|\,e,\,1\rangle\langle e,\,1\,|\hat{G}|\,e,\,1\rangle\langle e,\,1\,|\hat{V}_{\rm nr}|\,g,\,0\rangle = \Omega_{\rm R}^2\langle e,\,1\,|\hat{G}|\,e,\,1\rangle. \tag{B14}$$

In order to calculate $\Delta_0^{(2)}$, we observe that

$$\langle g,\,0\,|\hat{V}_{\rm nr}|\,e,\,1\rangle = \langle e,\,1\,|\hat{V}_{\rm nr}|\,g,\,0\rangle = \Omega_{\rm R}. \tag{B15}$$

The remaining term, $\langle e,\,1\,|\hat{G}|\,e,\,1\rangle$, is a convergent geometric series that is calculated in appendix E. We obtain

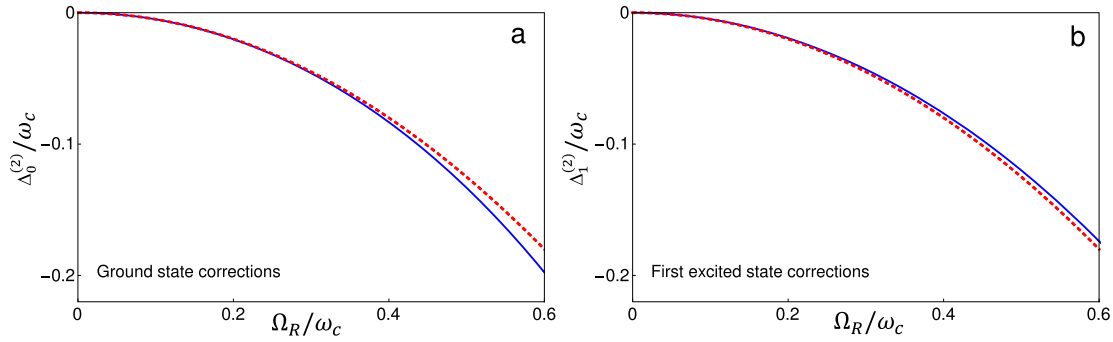

Figure B1. Comparison between the exact (numerical) and approximated (diagrammatic) calculation of the correction terms for (a) the ground-state energy and (b) the first excited state. The blue continuous lines describe the numerical calculation, while the red dotted lines describe the approximate one.

$$\Delta_0^{(2)} = \frac{\Omega_R^2}{2\omega_c}\frac{1}{\Omega_R^2/2\omega_c^2 - 1}. \tag{B16}$$

For $\Omega_R/\omega_c < 1$, $\Delta_0^{(2)}$ can be approximated to second order in Ω_R:

$$\Delta_0^{(2)} \approx -\frac{\Omega_R^2}{2\omega_c}. \tag{B17}$$

In figure B1, we show the comparison between the exact (numerical) and approximated (diagrammatic) calculation of the correction term to the ground state energy.

This approach can also be applied to the excited states. We consider the first excited state. Using equation (B10), we are able to calculate the correction up to second order in the potential $\hat{V}_{sg}$ to E_1; we have

$$\Delta_1^{(2)} = \langle \mathcal{E}_1^- \,|\hat{V}_{nr}\hat{G}(\mathcal{E}_1^-)\hat{V}_{nr}|\, \mathcal{E}_1^-\rangle = \mathcal{S}_1^2\langle g,\, 1\,|\hat{V}_{nr}\hat{G}(\mathcal{E}_1^-)\hat{V}_{nr}|\, g,\, 1\rangle. \tag{B18}$$

Observing that $\hat{V}_{nr}|e,\, 0\rangle = 0$, $\hat{V}_{nr}|g,\, 1\rangle = \sqrt{2}\,\Omega_R|e,\, 2\rangle$, and $|\mathcal{E}_1^-\rangle = -\mathcal{S}_1|g,\, 1\rangle + \mathcal{C}_1|e,\, 0\rangle$, we have

$$\hat{V}_{nr}|\mathcal{E}_1^-\rangle = -\sqrt{2}\,\mathcal{S}_1\Omega_R|e,\, 2\rangle. \tag{B19}$$

Equation (B18) becomes

$$\begin{aligned}\Delta_1^{(2)} &= \langle \mathcal{E}_1^- \,|\hat{V}_{nr}\hat{G}(\mathcal{E}_1^-)\hat{V}_{nr}|\, \mathcal{E}_1^-\rangle = \mathcal{S}_1^2\langle g,\, 1\,|\hat{V}_{nr}\hat{G}(\mathcal{E}_1^-)\hat{V}_{nr}|\, g,\, 1\rangle \\ &= 2\mathcal{S}_1^2\,\Omega_R^2\,\langle e,\, 0\,|\hat{G}(\mathcal{E}_1^-)|\, e,\, 0\rangle.\end{aligned} \tag{B20}$$

The energy correction $\Delta_1^{(2)}$ can be easily evaluated by directly using $\hat{G}(z)$ or by summing up the infinite contributions arising from the Dyson series, described by the diagrams (see appendix E, equation (E11)).

In the absence of detuning, we have for the first excited state

$$|\mathcal{E}_1^-\rangle = \frac{1}{\sqrt{2}}(-|g,\, 1\rangle + |e,\, 0\rangle), \tag{B21}$$

with energy

$$\mathcal{E}_1^- = \omega_c - \Omega_R. \tag{B22}$$

We obtain

$$\Delta_1^{(2)} = -\Omega_R^2\frac{\Omega_R + 2\omega_c}{4\omega_c^2 - 4\Omega_R\omega_c - 2\Omega_R^2}. \tag{B23}$$

For $\Omega_R/\omega_c < 1$, $\Delta_1^{(2)}$ can be approximated to second order in Ω_R:

$$\Delta_1^{(2)} \approx -\frac{\Omega_R^2}{2\omega_c}. \tag{B24}$$

A comparison between the approximate analytical energy corrections and the corresponding nonperturbative numerical calculations can be found in figure B1.

Appendix C. Additional perturbation $\hat{V}_{sg}$ allowing transitions from $|g\rangle$ to $|s\rangle$

Using equation (B1), the correction to the JC eigenstate $|\mathcal{E}_n\rangle$ up to the first order in the non-resonant potential becomes,

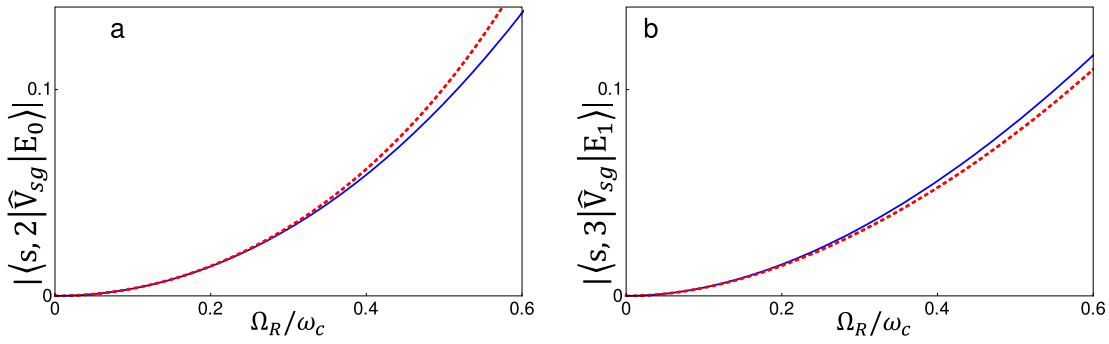

Figure C1. (a) Comparison between the exact (numerical, blue continuous curve) and approximated (diagrammatic, red dotted curve) calculation of the transition element $|\langle s,\,2|\hat{V}_{sg}|E_0\rangle$ between the state $|s,\,2\rangle$ (where $|s\rangle$ is now the real ground state) and $|E_0\rangle$ (the cavity-dressed ground state) due to the additional $\hat{V}_{sg}$ potential as a function of the coupling parameter normalised to the cavity resonance frequency. (b) Comparison between the exact (numerical) and approximated (diagrammatic) calculation of the transition element $|\langle s,\,3|\hat{V}_{sg}|E_1\rangle|$ between the state $|s,\,3\rangle$ (where $|s\rangle$ is now the real ground state) and $|E_1\rangle$ (the cavity-dressed first excited state) due to the additional $\hat{V}_{sg}$ potential as a function of the coupling parameter, normalised to the cavity resonance frequency. This comparison confirms the validity of the approximate diagrammatic approach. For the sake of simplicity, here we used $\Omega_R\mu_{sg}=1$.

$$|E_n^{(1)}\rangle = \hat{Q}_n\hat{G}(\mathcal{E}_n)\hat{V}_{\rm nr}|\mathcal{E}_n\rangle. \tag{C1}$$

We now consider the direct excitation of the artificial atom by applied electromagnetic pulses, described by the Hamiltonian

$$\hat{H}_{\rm d} = \mathcal{E}(t)(\hat{V}_{sg} + \hat{V}_{se}), \tag{C2}$$

where $\hat{V}_{sg} = \mu_{sg}(|g\rangle\langle s| + |s\rangle\langle g|)$, $\hat{V}_{se} = \mu_{se}(|e\rangle\langle s| + |s\rangle\langle e|)$, and μ_{sg} and μ_{se} are the dipole moments (here assumed to be real) for the transitions $|s\rangle \leftrightarrow |g\rangle$ and $|s\rangle \leftrightarrow |e\rangle$, respectively.

First, we consider the case with the system prepared in the state $|\mathcal{E}_0\rangle = |g,\,0\rangle$. The time-dependent perturbation can induce additional transitions whose rate can be evaluated with the Fermi golden rule.

In the absence of the counter-rotating interaction terms $\hat{V}_{\rm nr}$, $\hat{H}_{\rm d}$ can induce only zero-cavity-photon transitions $|g,\,0\rangle \leftrightarrow |s,\,0\rangle$. When including the counter-rotating terms, additional transitions are activated. For example, the transition $|E_0\rangle \leftrightarrow |s,\,2\rangle$ acquires a nonzero matrix element $\langle s,\,2\,|\hat{V}_{sg}|\,E_0\rangle$, where $|E_0\rangle$ is the lowest energy state of the Rabi Hamiltonian. It can be calculated perturbatively in $\hat{V}_{\rm nr}$, approximating $|E_0\rangle$ to first order in $\hat{V}_{\rm nr}$ (see equation (B3)):

$$|E_0\rangle \simeq |g,\,0\rangle + \hat{G}(\mathcal{E}_0)\hat{V}_{\rm nr}|g,\,0\rangle. \tag{C3}$$

We obtain

$$\langle s,\,2\,|\hat{V}_{sg}|\,E_0\rangle = \langle s,\,2\,|\hat{V}_{sg}\hat{G}(\mathcal{E}_0)\hat{V}_{\rm nr}|\,g,\,0\rangle = \Omega_{\rm R}\mu_{sg}\langle g,\,2\,|\hat{G}(\mathcal{E}_0)|\,e,\,1\rangle. \tag{C4}$$

The corresponding Dyson series is

$$\begin{aligned}\langle g,\,2\,|\hat{G}(\mathcal{E}_0)|\,e,\,1\rangle &= \langle g,\,2\,|\hat{G}_0(\mathcal{E}_0)|\,e,\,1\rangle + \langle g,\,2\,|\hat{G}_0(\mathcal{E}_0)\hat{V}_{\rm r}\hat{G}_0(\mathcal{E}_0)|\,e,\,1\rangle + \ldots \\ &= \frac{\sqrt{2}\,\Omega_{\rm R}}{(\mathcal{E}_0 - 2\omega_{\rm c})^2 - 2\Omega_{\rm R}^2} = \frac{\sqrt{2}\,\Omega_{\rm R}}{4\omega_{\rm c}^2 - 2\Omega_{\rm R}^2}.\end{aligned} \tag{C5}$$

The comparison between the exact (numerical) and approximated (diagrammatic) calculation of this matrix element is shown in figure C1.

We now consider the case with the system prepared in the state $|\mathcal{E}_1^-\rangle = \frac{1}{\sqrt{2}}(-|g,\,1\rangle + |e,\,0\rangle)$, whose energy is $\mathcal{E}_1^- = \omega_{\rm c} - \Omega_{\rm R}$. The time-dependent perturbation can induce additional transitions whose rate can be evaluated with the Fermi golden rule. In the presence of $\hat{V}_{\rm nr}$, additional transitions, such as $|E_1\rangle \leftrightarrow |s,\,3\rangle$, become activated. The matrix element for this transition is $\langle s,\,3\,|\hat{V}_{sg}|\,E_1\rangle$. It can be calculated perturbatively in $\hat{V}_{\rm nr}$, approximating $|E_1\rangle$ to first order in $\hat{V}_{\rm nr}$ (see equation (B3)):

$$|E_1\rangle \simeq |\mathcal{E}_1^-\rangle + \hat{G}(\mathcal{E}_1^-)\hat{V}_{\rm nr}|\mathcal{E}_1^-\rangle. \tag{C6}$$

Observing that

$$\hat{V}_{\rm nr}|\mathcal{E}_1^-\rangle = -\frac{1}{\sqrt{2}}(\hat{V}_{\rm nr}|g,\,1\rangle - \hat{V}_{\rm nr}|e,\,0\rangle) = -\Omega_{\rm R}|e,\,2\rangle, \tag{C7}$$

where we have used the relations $\hat{V}_{\rm nr}|g,\,1\rangle = \sqrt{2}\,\Omega_{\rm R}|e,\,2\rangle$ and $\hat{V}_{\rm nr}|e,\,0\rangle = 0$, we obtain

$$\langle s,\,3\,|\hat{V}_{sg}|\,E_1\rangle = \langle s,\,3\,|\hat{V}_{sg}\hat{G}(\mathcal{E}_1^-)\hat{V}_{\rm nr}|\,\mathcal{E}_1^-\rangle = -\Omega_{\rm R}\mu_{sg}\,\langle g,\,3\,|\hat{G}(\mathcal{E}_1^-)|\,e,\,2\rangle. \tag{C8}$$

The corresponding Dyson series is (see appendix E and equation (E12))

$$\begin{aligned}\langle g,\,3\,|\hat{G}(\mathcal{E}_1^-)|\,e,\,2\rangle &= \langle g,\,3\,|\hat{G}_0(\mathcal{E}_1^-)|\,e,\,2\rangle + \langle g,\,3\,|\hat{G}_0(\mathcal{E}_1^-)\hat{V}_{\rm r}\hat{G}_0(\mathcal{E}_1^-)|\,e,\,2\rangle + \ldots \\ &= \frac{\sqrt{3}\,\Omega_{\rm R}}{(\mathcal{E}_1 - 3\omega_{\rm c})^2 - 3\Omega_{\rm R}^2} = \frac{\sqrt{3}\,\Omega_{\rm R}}{(\Omega_{\rm R} + 2\omega_{\rm c})^2 - 3\Omega_{\rm R}^2}.\end{aligned} \tag{C9}$$

Appendix D. Additional perturbation $\hat{V}_{se}$ allowing transitions from $|e\rangle$ to $|s\rangle$

We now consider a situation similar to the one analysed previously. In this case, a transition $|s\rangle \leftrightarrow |e\rangle$ is detuned at a much higher energy than the cavity resonance. The part of the time-dependent potential inducing the $|s\rangle \leftrightarrow |e\rangle$ transitions is $\hat{V}'(t) = \mathcal{E}(t)\,\hat{V}_{se}$. In the absence of the counter-rotating interaction terms $\hat{V}_{\rm nr}$, $\hat{V}'(t)$ can induce zero-cavity-photon transitions $|e,\,0\rangle \leftrightarrow |s,\,0\rangle$.

In the presence of $\hat{V}_{\rm nr}$, additional transitions, such as $|E_0\rangle \leftrightarrow |s,\,1\rangle$, can be activated. The matrix element for this transition is $\langle s,\,1\,|\hat{V}_{se}|\,E_0\rangle$. It can be calculated perturbatively in $\hat{V}_{\rm nr}$, approximating $|E_0\rangle$ to the first order in $\hat{V}_{\rm nr}$ (see equation (B3)):

$$|E_0\rangle \simeq |g,\,0\rangle + \hat{G}(\mathcal{E}_0)\hat{V}_{\rm nr}|g,\,0\rangle. \tag{D1}$$

We have

$$\langle s,\,1\,|\hat{V}_{se}|\,E_0\rangle = \langle s,\,1\,|\hat{V}_{se}\hat{G}_0(\mathcal{E}_0)\hat{V}_{\rm nr}|\,g,\,0\rangle = \Omega_{\rm R}\mu_{se}\,\langle e,\,1\,|\hat{G}_0(\mathcal{E}_0)|\,e,\,1\rangle. \tag{D2}$$

Exploiting the Dyson series for the Green's function, we obtain

$$\langle e,\,1\,|\hat{G}(\mathcal{E}_0)|\,e,\,1\rangle = \langle e,\,1\,|\hat{G}_0(\mathcal{E}_0)|\,e,\,1\rangle + \langle e,\,1\,|\hat{G}_0(\mathcal{E}_0)\hat{V}_{\rm r}\hat{G}_0(\mathcal{E}_0)|\,e,\,1\rangle + \ldots. \tag{D3}$$

In this series, owing to the nature of the resonant potential, only the odd terms are non-zero. We have:

$$\langle e,\,1\,|\hat{G}(\mathcal{E}_0)|\,e,\,1\rangle = \langle e,\,1\,|\hat{G}_0(\mathcal{E}_0)|\,e,\,1\rangle + \sum_{n=1}^{\infty}\langle e,\,1\,|\hat{G}_0(\mathcal{E}_0)(\hat{V}_{\rm r}\hat{G}_0(\mathcal{E}_0))^{2n}|\,e,\,1\rangle. \tag{D4}$$

The diagrammatic analysis of this process is shown in figure 5 of the main part of the paper. Using the results of appendix E, the Dyson series calculation of equation (D2), at resonance ($\omega_{\rm c} \simeq \omega_{eg}$), gives

$$\langle s,\,1\,|\hat{V}_{se}|\,E_0\rangle = \Omega_{\rm R}\mu_{se}\,\langle e,\,1\,|\hat{G}(\mathcal{E}_0)|\,e,\,1\rangle = \mu_{se}\frac{\Omega_{\rm R}\omega_{\rm c}}{\Omega_{\rm R}^2 - 2\omega_{\rm c}^2}. \tag{D5}$$

Appendix E. Calculation of the $\hat{G}$ matrix elements using the Dyson equation

In this section, we perform all the calculations for the determination of the correction to the self-energy to second order in $\hat{V}_{\rm nr}$. We have to sum all the elements of the infinite series. The generic matrix element is

$$\langle e,\,1\,|\hat{G}_0(z)[\hat{V}_{\rm r}\hat{G}_0(z)]^n|\,e,\,1\rangle. \tag{E1}$$

We observe that the matrix element will be zero if $\hat{V}_{\rm r}$ appears an odd number of times, i.e.,

$$\langle e,\,1\,|\hat{G}_0(z)[\hat{V}_{\rm r}\hat{G}_0(z)]^{2n+1}|\,e,\,1\rangle = 0 \qquad \text{for } n > 0. \tag{E2}$$

Hence we may perform the calculation for the self-energy considering only the even-power terms. In addition, we observe that

$$\langle g,\,n+1\,|\hat{V}_{\rm r}|\,e,\,n\rangle = \langle e,\,n\,|\hat{V}_{\rm r}|\,g,\,n+1\rangle = \sqrt{n+1}\;\Omega_{\rm R}. \tag{E3}$$

We then obtain

$$\begin{aligned}\langle e,\,1\,|\hat{G}|\,e,\,1\rangle &= \sum_{n=0}^{\infty}\langle e,\,1\,|\hat{G}_0(z)[\hat{V}_{\rm r}\hat{G}_0(z)]^{2n}|\,e,\,1\rangle\\ &= \langle e,\,1\,|\hat{G}_0(z)|\,e,\,1\rangle\sum_{n=0}^{\infty}\langle e,\,1\,|[\hat{V}_{\rm r}\hat{G}_0(z)]^{2n}|\,e,\,1\rangle\\ &= \langle e,\,1\,|\hat{G}_0(z)|\,e,\,1\rangle\sum_{n=0}^{\infty}|\langle e,\,1\,|\hat{V}_{\rm r}|\,g,\,2\rangle|^{2n}(\langle e,\,1\,|\hat{G}_0(z)|\,e,\,1\rangle)^n(\langle g,\,2\,|\hat{G}_0(z)|\,g,\,2\rangle)^n\\ &= \langle e,\,1\,|\hat{G}_0(z)|\,e,\,1\rangle\sum_{n=0}^{\infty}(\sigma)^n,\end{aligned} \tag{E4}$$

where

$$\begin{aligned}\sigma &= |\langle e,\,1\,|\hat{V}_{\rm r}|\,g,\,2\rangle|^2\langle e,\,1\,|\hat{G}_0(z)|\,e,\,1\rangle\\ &= 2\Omega_{\rm R}^2\langle e,\,1\,|\hat{G}_0(z)|\,e,\,1\rangle\langle g,\,2\,|\hat{G}_0(z)|\,g,\,2\rangle.\end{aligned} \tag{E5}$$

Following [72], the Green's function operator relative to a generic differential operator $\hat{L}$ satisfies the relation

$$[z-\hat{L}]\hat{G}(z)=\hat{I}, \tag{E6}$$

with z a convenient parameter. Therefore, for the cases $\hat{L}=\hat{H}$ and $\hat{L}=\hat{H}_0$, we have, respectively:

$$\hat{G}(z)=[z-\hat{H}]^{-1},\quad \hat{G}_0(z)=[z-\hat{H}_0]^{-1}. \tag{E7}$$

In our calculation, we choose $z=\mathcal{E}_0$ (hence $\hat{G}_0(z)$ is the resolvent of the free Hamiltonian eigenvalue problem):

$$\begin{aligned}\langle e,\,1\,|\hat{G}(z)|\,e,\,1\rangle &= \langle e,\,1\,|\hat{G}_0(z)|\,e,\,1\rangle\frac{1}{1-\sigma}=\frac{(\langle g,\,2\,|\hat{G}_0(z)|\,g,\,2\rangle)^{-1}}{(\langle e,\,1\,|\hat{G}_0(z)|\,e,\,1\rangle)^{-1}(\langle g,\,2\,|\hat{G}_0(z)|\,g,\,2\rangle)^{-1}-2\Omega_{\rm R}^2}\\ &= \frac{(z-2\omega_{\rm c})}{(z-\omega_{eg}-\omega_{\rm c})(z-2\omega_{\rm c})-2\Omega_{\rm R}^2}.\end{aligned} \tag{E8}$$

For the sake of completeness, we now calculate the other non-zero matrix elements:

$$\begin{aligned}\langle e,\,1\,|\hat{G}(z)|\,g,\,2\rangle &= \sum_{n=0}^{\infty}\langle e,\,1\,|\hat{G}_0(z)[\hat{V}_{\rm r}\hat{G}_0(z)]^{2n+1}|\,g,\,2\rangle\\ &= \langle g,\,2\,|\hat{G}_0(z)|\,g,\,2\rangle\langle e,\,1\,|\hat{G}_0(z)|\,e,\,1\rangle\langle e,\,1\,|\hat{V}_{\rm r}|\,g,\,2\rangle\sum_{n=0}^{\infty}\langle e,\,1\,|[\hat{V}_{\rm r}\hat{G}_0(z)]^{2n}|\,e,\,1\rangle\\ &= \langle g,\,2\,|\hat{G}_0(z)|\,g,\,2\rangle\langle e,\,1\,|\hat{V}_{\rm r}|\,g,\,2\rangle\langle e,\,1\,|\hat{G}(z)|\,e,\,1\rangle\\ &= \langle g,\,2\,|\hat{G}_0(z)|\,g,\,2\rangle\langle e,\,1\,|\hat{V}_{\rm r}|\,g,\,2\rangle\langle e,\,1\,|\hat{G}_0(z)|\,e,\,1\rangle\sum_{n=0}^{\infty}(\sigma)^n\\ &= \langle e,\,1\,|\hat{G}_0(z)|\,e,\,1\rangle\langle g,\,2\,|\hat{G}_0(z)|\,g,\,2\rangle\frac{\sqrt{2}\,\Omega_{\rm R}}{1-\sigma}\\ &= \frac{\sqrt{2}\,\Omega_{\rm R}}{(\langle e,\,1\,|\hat{G}_0(z)|\,e,\,1\rangle)^{-1}(\langle g,\,2\,|\hat{G}_0(z)|\,g,\,2\rangle)^{-1}-2\Omega_{\rm R}^2}\\ &= \frac{\sqrt{2}\,\Omega_{\rm R}}{(z-\omega_{eg}-\omega_{\rm c})(z-2\omega_{\rm c})-2\Omega_{\rm R}^2}\end{aligned} \tag{E9}$$

and

$$\begin{aligned}\langle g,\,2\,|\hat{G}(z)|\,g,\,2\rangle &= \langle g,\,2\,|\hat{G}_0(z)|\,g,\,2\rangle\frac{1}{1-\sigma}\\ &= \frac{(\langle e,\,1\,|\hat{G}(z)|\,e,\,1\rangle)^{-1}}{(\langle e,\,1\,|\hat{G}_0(z)|\,e,\,1\rangle)^{-1}(\langle g,\,2\,|\hat{G}_0(z)|\,g,\,2\rangle)^{-1}-2\Omega_{\rm R}^2}\\ &= \frac{(z-\omega_{eg}-\omega_{\rm c})}{(z-\omega_{eg}-\omega_{\rm c})(z-2\omega_{\rm c})-2\Omega_{\rm R}^2}.\end{aligned} \tag{E10}$$

The generalisation of the above matrix elements to all n subspaces is straightforward. Actually, all the contributions of the self-energy can be easily calculated because the JC Hamiltonian divides the entire Hilbert space into disjoint 2D subspaces (labelled by n) spanned by $(|e,\ n\rangle, |g,\ n+1\rangle)$. For the generic nth subspace we have

$$\langle e,\ n\ |\hat{G}(z)|\ e,\ n\rangle = \frac{(z-(n+1)\omega_c)}{(z-\omega_{eg}-n\omega_c)(z-(n+1)\omega_c)-(n+1)\Omega_R^2}, \tag{E11}$$

$$\langle e,\ n\ |\hat{G}(z)|\ g,\ n+1\rangle = \frac{\sqrt{n+1}\,\Omega_R}{(z-\omega_{eg}-n\omega_c)(z-(n+1)\omega_c)-(n+1)\Omega_R^2}, \tag{E12}$$

$$\langle g,\ n+1\ |\hat{G}(z)|\ g,\ n+1\rangle = \frac{(z-\omega_{eg}-n\omega_c)}{(z-\omega_{eg}-n\omega_c)(z-(n+1)\omega_c)-(n+1)\Omega_R^2}. \tag{E13}$$

References

[1] Peskin M E and Schroeder D V 1995 *An Introduction to Quantum Field Theory* (Boulder, CO: Westview Press)
[2] Maggiore M 2004 *A Modern Introduction to Quantum Field Theory* (Oxford: Oxford University Press)
[3] Lamb W E and Retherford R C 1947 Fine structure of the hydrogen atom by a microwave method *Phys. Rev.* **72** 241
[4] Bethe H A 1947 The electromagnetic shift of energy levels *Phys. Rev.* **72** 339
[5] Schwinger J 1948 On quantum-electrodynamics and the magnetic moment of the electron *Phys. Rev.* **73** 416
[6] Welton T A 1948 Some observable effects of the quantum-mechanical fluctuations of the electromagnetic field *Phys. Rev.* **74** 1157
[7] Stassi R, Ridolfo A, Di Stefano O, Hartmann M J and Savasta S 2013 Spontaneous conversion from virtual to real photons in the ultrastrong-coupling regime *Phys. Rev. Lett.* **110** 243601
[8] Garziano L, Stassi R, Ridolfo A, Di Stefano O and Savasta S 2014 Vacuum-induced symmetry breaking in a superconducting quantum circuit *Phys. Rev.* A **90** 043817
[9] Haroche S 2013 Nobel lecture: controlling photons in a box and exploring the quantum to classical boundary *Rev. Mod. Phys.* **85** 1083
[10] Felicetti S, Douce T, Romero G, Milman P and Solano E 2015 Parity-dependent state engineering and tomography in the ultrastrong coupling regime *Sci. Rep.* **5** 11818
[11] Dimer F, Estienne B, Parkins A S and Carmichael H J 2007 Proposed realization of the Dicke-model quantum phase transition in an optical cavity QED system *Phys. Rev.* A **75** 013804
[12] De Liberato S, Ciuti C and Carusotto I 2007 Quantum vacuum radiation spectra from a semiconductor microcavity with a time-modulated vacuum rabi frequency *Phys. Rev. Lett.* **98** 103602
[13] Cao X, You J Q, Zheng H, Kofman A G and Nori F 2010 Dynamics and quantum Zeno effect for a qubit in either a low- or high-frequency bath beyond the rotating-wave approximation *Phys. Rev.* A **82** 022119
[14] Cao X, You J Q, Zheng H and Nori F 2011 A qubit strongly coupled to a resonant cavity: asymmetry of the spontaneous emission spectrum beyond the rotating wave approximation *New J. Phys.* **13** 073002
[15] Ridolfo A, Leib M, Savasta S and Hartmann M J 2012 Photon blockade in the ultrastrong coupling regime *Phys. Rev. Lett.* **109** 193602
[16] Ridolfo A, Savasta S and Hartmann M J 2013 Nonclassical radiation from thermal cavities in the ultrastrong coupling regime *Phys. Rev. Lett.* **110** 163601
[17] Sanchez-Burillo E, Zueco D, Garcia-Ripoll J J and Martin-Moreno L 2014 Scattering in the ultrastrong regime: nonlinear optics with one photon *Phys. Rev. Lett.* **113** 263604
[18] Cacciola A, Di Stefano O, Stassi R, Saija R and Savasta S 2014 Ultrastrong coupling of plasmons and excitons in a nanoshell *ACS Nano* **8** 11483
[19] Lolli J, Baksic A, Nagy D, Manucharyan V E and Ciuti C 2015 Ancillary qubit spectroscopy of vacua in cavity and circuit quantum electrodynamics *Phys. Rev. Lett.* **114** 183601
[20] Garziano L, Stassi R, Macrì V, Kockum A F, Savasta S and Nori F 2015 Multiphoton quantum Rabi oscillations in ultrastrong cavity QED *Phys. Rev.* A **92** 063830
[21] Garziano L, Stassi R, Macrì V, Di Stefano O, Nori F and Savasta S 2016 One photon can simultaneously excite two or more atoms *Phys. Rev. Lett.* **117** 043601
[22] Kockum A F, Miranowicz A, Macrì V, Savasta S and Nori F 2017 Deterministic quantum nonlinear optics with single atoms and virtual photons arXiv:1701.05038
[23] Forn-Díaz P, Lisenfeld J, Marcos D, García-Ripoll J J, Solano E, Harmans C J P M and Mooij J E 2010 Observation of the bloch-siegert shift in a qubit-oscillator system in the ultrastrong coupling regime *Phys. Rev. Lett.* **105** 237001
[24] Niemczyk T *et al* 2010 Circuit quantum electrodynamics in the ultrastrong-coupling regime *Nat. Phys.* **6** 772
[25] Todorov Y, Andrews A M, Colombelli R, De Liberato S, Ciuti C, Klang P, Strasser G and Sirtori C 2010 Ultrastrong light–matter coupling regime with polariton dots *Phys. Rev. Lett.* **105** 196402
[26] Schwartz T, Hutchison J A, Genet C and Ebbesen T W 2011 Reversible switching of ultrastrong light-molecule coupling *Phys. Rev. Lett.* **106** 196405
[27] Scalari G *et al* 2012 Ultrastrong coupling of the cyclotron transition of a 2D electron gas to a THz metamaterial *Science* **335** 1323
[28] Geiser M, Castellano F, Scalari G, Beck M, Nevou L and Faist J 2012 Ultrastrong coupling regime and plasmon polaritons in parabolic semiconductor quantum wells *Phys. Rev. Lett.* **108** 106402
[29] Kéna-Cohen S, Maier S A and Bradley D D C 2013 Ultrastrongly coupled exciton-polaritons in metal-clad organic semiconductor microcavities *Adv. Opt. Mater.* **1** 827
[30] Gambino S *et al* 2014 Exploring light–matter interaction phenomena under ultrastrong coupling regime *ACS Photon.* **1** 1042
[31] Mazzeo M, Genco A, Gambino S, Ballarini D, Mangione F, Di Stefano O, Patanè S, Savasta S, Sanvitto D and Gigli G 2014 Ultrastrong light–matter coupling in electrically doped microcavity organic light emitting diodes *Appl. Phys. Lett.* **104** 86_1
[32] Maissen C, Scalari G, Valmorra F, Beck M, Faist J, Cibella S, Leoni R, Reichl C, Charpentier C and Wegscheider W 2014 Ultrastrong coupling in the near field of complementary split-ring resonators *Phys. Rev.* B **90** 205309

[33] Goryachev M, Farr W G, Creedon D L, Fan Y, Kostylev M and Tobar M E 2014 High-cooperativity cavity QED with magnons at microwave frequencies *Phys. Rev. Appl.* **2** 054002
[34] Haeberlein M *et al* 2015 Spin-boson model with an engineered reservoir in circuit quantum electrodynamics arXiv:1506.09114
[35] Yoshihara F, Fuse T, Ashhab S, Kakuyanagi K, Saito S and Semba K 2017 Superconducting qubit-oscillator circuit beyond the ultrastrong-coupling regime *Nat. Phys.* **13** 44–7
[36] Forn-Díaz P, García-Ripoll J J, Peropadre B, Orgiazzi J-L, Yurtalan M A, Belyansky R, Wilson C M and Lupascu A 2017 Ultrastrong coupling of a single artificial atom to an electromagnetic continuum in the nonperturbative regime *Nat. Phys.* **13** 39–43
[37] Chen Z *et al* 2016 Multi-photon sideband transitions in an ultrastrongly-coupled circuit quantum electrodynamics system arXiv:1602.01584
[38] Ciuti C and Carusotto I 2006 Input–output theory of cavities in the ultrastrong coupling regime: the case of time-independent cavity parameters *Phys. Rev.* A **74** 033811
[39] Ashhab S and Nori F 2010 Qubit-oscillator systems in the ultrastrong-coupling regime and their potential for preparing nonclassical states *Phys. Rev.* A **81** 042311
[40] Garziano L, Ridolfo A, Stassi R, Di Stefano O and Savasta S 2013 Switching on and off of ultrastrong light–matter interaction: photon statistics of quantum vacuum radiation *Phys. Rev.* A **88** 063829
[41] Savasta S and Girlanda R 1996 Quantum description of the input and output electromagnetic fields in a polarizable confined system *Phys. Rev.* A **53** 2716
[42] Huang J-F and Law C K 2014 Photon emission via vacuum-dressed intermediate states under ultrastrong coupling *Phys. Rev.* A **89** 033827
[43] Cirio M, De Liberato S, Lambert N and Nori F 2016 Ground state electroluminescence *Phys. Rev. Lett.* **116** 113601
[44] Moore G T 1970 Quantum theory of the electromagnetic field in a variable-length one-dimensional cavity *J. Math. Phys.* **11** 2679
[45] Johansson J R, Johansson G, Wilson C M and Nori F 2009 Dynamical Casimir effect in a superconducting coplanar waveguide *Phys. Rev. Lett.* **103** 147003
[46] Johansson J R, Johansson G, Wilson C M and Nori F 2010 Dynamical Casimir effect in superconducting microwave circuits *Phys. Rev.* A **82** 52509
[47] Johansson J R, Johansson G, Wilson C M, Delsing P and Nori F 2013 Nonclassical microwave radiation from the dynamical Casimir effect *Phys. Rev.* A **87** 043804
[48] Wilson C M, Johansson G, Pourkabirian A, Simoen M, Johansson J R, Duty T, Nori F and Delsing P 2011 Observation of the dynamical Casimir effect in a superconducting circuit *Nature* **479** 376
[49] de Sousa I M and Dodonov A V 2015 Microscopic toy model for the cavity dynamical Casimir effect *J. Phys. A: Math. Theor.* **48** 245302
[50] Rabi I I 1937 Space quantization in a gyrating magnetic field *Phys. Rev.* **51** 652
[51] Braak D 2011 Integrability of the Rabi model *Phys. Rev. Lett.* **107** 100401
[52] Cohen-Tannoudji C, Dupont-Roc J and Grynberg G 1998 *Atom-Photon Interactions* (New York: Wiley)
[53] Einstein A 1917 Zur Quantentheorie der strahlung *Phys. Z.* **18** 121
[54] Jaynes E T and Cummings F W 1963 Comparison of quantum and semiclassical radiation theories with application to the beam maser *Proc. IEEE* **51** 89
[55] Emary C and Brandes T 2003 Chaos and the quantum phase transition in the dicke model *Phys. Rev.* E **67** 066203
[56] Casanova J, Romero G, Lizuain I, García-Ripoll J J and Solano E 2010 Deep strong coupling regime of the Jaynes–Cummings model *Phys. Rev. Lett.* **105** 263603
[57] Crespi A, Longhi S and Osellame R 2012 Photonic realization of the quantum Rabi model *Phys. Rev. Lett.* **108** 163601
[58] Konishi K and Paffuti G 2009 *Quantum Mechanics: A New Introduction* (Oxford: Oxford University Press)
[59] Ridolfo A, Vilardi R, Di Stefano O, Portolan S and Savasta S 2011 All optical switch of vacuum Rabi oscillations: the ultrafast quantum eraser *Phys. Rev. Lett.* **106** 013601
[60] Carusotto I, De Liberato S, Gerace D and Ciuti C 2012 Back-reaction effects of quantum vacuum in cavity quantum electrodynamics *Phys. Rev.* A **85** 023805
[61] Liu Y-X, You J Q, Wei L F, Sun C P and Nori F 2005 Optical selection rules and phase-dependent adiabatic state control in a superconducting quantum circuit *Phys. Rev. Lett.* **95** 087001
[62] Breuer H-P and Petruccione F 2002 *The Theory of Open Quantum Systems* (Oxford: Oxford University Press)
[63] Beaudoin F, Gambetta J M and Blais A 2011 Dissipation and ultrastrong coupling in circuit QED *Phys. Rev.* A **84** 043832
[64] Yan F *et al* 2016 The flux qubit revisited to enhance coherence and reproducibility *Nat. Commun.* **7** 12964
[65] You J Q and Nori F 2011 Atomic physics and quantum optics using superconducting circuits *Nature* **474** 589–97
[66] Bourassa J, Gambetta J M, Abdumalikov A A, Astafiev O, Nakamura Y and Blais A 2009 Ultrastrong coupling regime of cavity QED with phase-biased flux qubits *Phys. Rev.* A **80** 032109
[67] Baust A *et al* 2016 Ultrastrong coupling in two-resonator circuit QED *Phys. Rev.* B **93** 214501
[68] Xiang Z-L, Ashhab S, You J Q and Nori F 2013 Hybrid quantum circuits: superconducting circuits interacting with other quantum systems *Rev. Mod. Phys.* **85** 623
[69] Günter G *et al* 2009 Sub-cycle switch-on of ultrastrong light–matter interaction *Nature* **458** 178
[70] Buluta I and Nori F 2009 Quantum simulators *Science* **326** 108–11
[71] Georgescu I M, Ashhab S and Nori F 2014 Quantum simulation *Rev. Mod. Phys.* **86** 153
[72] Economou E N 1984 *Green's Functions in Quantum Physics* vol 3 (Berlin: Springer)